ARTICLE

doi:10.1038/nature10915

Global warming preceded by increasing carbon dioxide concentrations during the last deglaciation

Jeremy D. Shakun[1,2], Peter U. Clark[3], Feng He[4], Shaun A. Marcott[3], Alan C. Mix[3], Zhengyu Liu[4,5,6], Bette Otto-Bliesner[7], Andreas Schmittner[3] & Edouard Bard[8]

The covariation of carbon dioxide (CO_2) concentration and temperature in Antarctic ice-core records suggests a close link between CO_2 and climate during the Pleistocene ice ages. The role and relative importance of CO_2 in producing these climate changes remains unclear, however, in part because the ice-core deuterium record reflects local rather than global temperature. Here we construct a record of global surface temperature from 80 proxy records and show that temperature is correlated with and generally lags CO_2 during the last (that is, the most recent) deglaciation. Differences between the respective temperature changes of the Northern Hemisphere and Southern Hemisphere parallel variations in the strength of the Atlantic meridional overturning circulation recorded in marine sediments. These observations, together with transient global climate model simulations, support the conclusion that an antiphased hemispheric temperature response to ocean circulation changes superimposed on globally in-phase warming driven by increasing CO_2 concentrations is an explanation for much of the temperature change at the end of the most recent ice age.

Understanding the causes of the Pleistocene ice ages has been a significant question in climate dynamics since they were discovered in the mid-nineteenth century. The identification of orbital frequencies in the marine $^{18}O/^{16}O$ record, a proxy for global ice volume, in the 1970s demonstrated that glacial cycles are ultimately paced by astronomical forcing[1]. Initial measurements of air bubbles in Antarctic ice cores in the 1980s revealed that greenhouse gas concentrations also increased and decreased over the last glacial cycle[2,3], suggesting they too may be part of the explanation. The ice-core record now extends back 800,000 yr and shows that local Antarctic temperature was strongly correlated with and seems to have slightly led changes in CO_2 concentration[4]. The implication of this relationship for understanding the role of CO_2 in glacial cycles, however, remains unclear. For instance, proxy data have variously been interpreted to suggest that CO_2 was the primary driver of the ice ages[5], a more modest feedback on warming[6,7] or, perhaps, largely a consequence rather than cause of past climate change[8]. Similarly, although climate models generally require greenhouse gases to explain globalization of the ice-age signal, they predict a wide range (one-third to two-thirds) in the contribution of greenhouse gases to ice-age cooling, with additional contributions from ice albedo and other effects[9,10]. Moreover, models have generally used prescribed forcings to simulate snapshots in time and thus by design do not distinguish the timing of changes in various forcings relative to responses.

Global temperature reconstructions and transient model simulations spanning the past century and millennium have been essential to the attribution of recent climate change, and a similar strategy would probably improve our understanding of glacial cycle dynamics. Here we use a network of proxy temperature records that provide broad spatial coverage to show that global temperature closely tracked the increase in CO_2 concentration over the last deglaciation, and that variations in the Atlantic meridional overturning circulation (AMOC) caused a seesawing of heat between the hemispheres, supporting an early hypothesis that identified potentially important roles for these mechanisms[11]. These findings, supported by transient simulations with a coupled ocean–atmosphere general circulation model, can explain the lag of CO_2 behind Antarctic temperature in the ice-core record and are consistent with an important role for CO_2 in driving global climate change over glacial cycles.

Global temperature

We calculate the area-weighted mean of 80 globally distributed, high-resolution proxy temperature records to reconstruct global surface temperature during the last deglaciation (Methods and Fig. 1). The global temperature stack shows a two-step rise, with most warming occurring during and right after the Oldest Dryas and Younger Dryas intervals and relatively little temperature change during the Last Glacial Maximum (LGM), the Bølling–Allerød interval and the early Holocene epoch (Fig. 2a). The atmospheric CO_2 record from the EPICA Dome C ice core[12], which has recently been placed on a more accurate timescale[13], has a similar two-step structure and is strongly correlated with the temperature stack ($r^2 = 0.94$ (coefficient of determination), $P = 0.03$; Fig. 2a).

Lag correlations quantify the timing of change in the temperature stack relative to CO_2 from 20–10 kyr ago, an interval that spans the period during which low LGM CO_2 concentrations increased to almost pre-industrial values. Our results indicate that CO_2 probably leads global warming over the course of the deglaciation (Fig. 2b). A comparison of the global temperature stack with Antarctic temperature provides further support for this relative timing, in showing that

[1]Department of Earth and Planetary Sciences, Harvard University, Cambridge, Massachusetts 02138, USA. [2]Lamont-Doherty Earth Observatory, Columbia University, Palisades, New York 10964, USA. [3]College of Earth, Ocean, and Atmospheric Sciences, Oregon State University, Corvallis, Oregon 97331, USA. [4]Center for Climatic Research, University of Wisconsin, Madison, Wisconsin 53706, USA. [5]Department of Atmospheric and Oceanic Sciences, University of Wisconsin, Madison, Wisconsin 53706, USA. [6]Laboratory for Ocean-Atmosphere Studies, Peking University, Beijing 100871, China. [7]Climate and Global Dynamics Division, National Center for Atmospheric Research, Boulder, Colorado 80307-3000, USA. [8]CEREGE, Collège de France, CNRS-Université Aix-Marseille, Europole de l'Arbois, 13545 Aix-en-Provence, France.

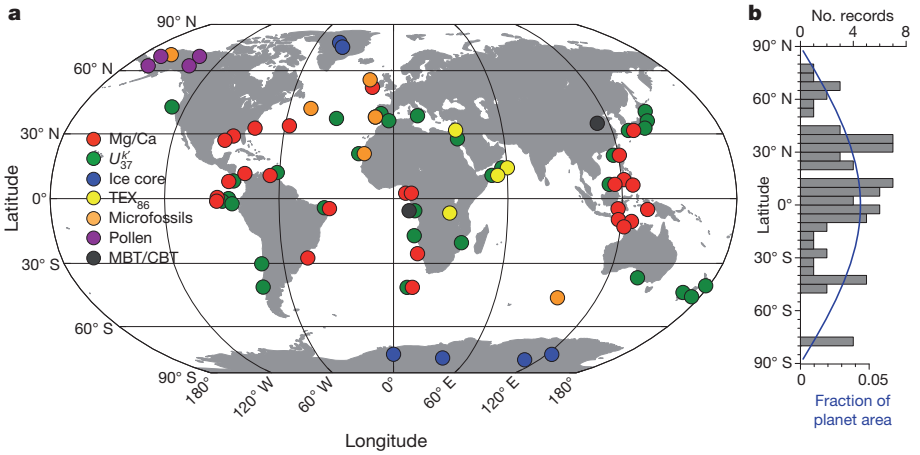

Figure 1 | Proxy temperature records. **a**, Location map. CBT, cyclization ratio of branched tetraethers; MBT, methylation index of branched tetraethers; TEX_{86}, tetraether index of tetraethers consisting of 86 carbon atoms; $U^{K'}_{37}$, alkenone unsaturation index. **b**, Distribution of the records by latitude (grey histogram) and areal fraction of the planet in 5° steps (blue line).

although the structure of the global stack is similar to the pattern of Antarctic temperature change, it lags Antarctica by several centuries to a millennium throughout most of the deglaciation (Fig. 2a). Thus, the small apparent lead of Antarctic temperature over CO_2 in the ice-core records[12,14] does not apply to global temperature. An additional evaluation of this result comes from an objective identification of inflection points in the CO_2 and global temperature records, which suggests that changes in CO_2 concentration were either synchronous with or led global warming during the various steps of the deglaciation (Supplementary Table 2). An important exception is the onset of deglaciation, which features about 0.3 °C of global warming before the initial increase in CO_2 ~17.5 kyr ago. This finding suggests that CO_2 was not the cause of initial warming. We return to this point below. Nevertheless, the overall correlation and phasing of global temperature and CO_2 are consistent with CO_2 being an important driver of global warming during the deglaciation, with the centennial-scale lag of temperature behind CO_2 being consistent with the thermal inertia of the climate system owing to ocean heat uptake and ice melting[15].

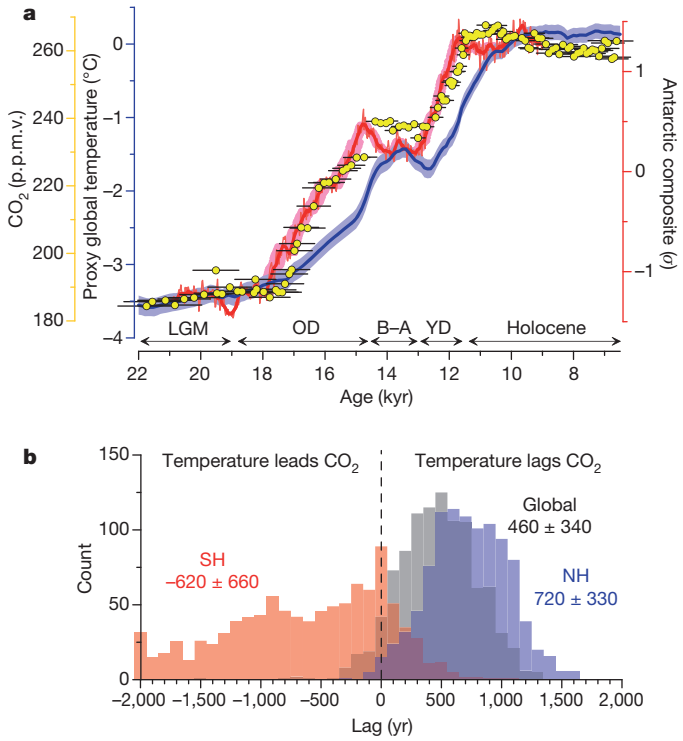

Figure 2 | CO_2 concentration and temperature. **a**, The global proxy temperature stack (blue) as deviations from the early Holocene (11.5–6.5 kyr ago) mean, an Antarctic ice-core composite temperature record[42] (red), and atmospheric CO_2 concentration (refs 12, 13; yellow dots). The Holocene, Younger Dryas (YD), Bølling–Allerød (B–A), Oldest Dryas (OD) and Last Glacial Maximum (LGM) intervals are indicated. Error bars, 1σ (Methods); p.p.m.v., parts per million by volume. **b**, The phasing of CO_2 concentration and temperature for the global (grey), Northern Hemisphere (NH; blue) and Southern Hemisphere (SH; red) proxy stacks based on lag correlations from 20–10 kyr ago in 1,000 Monte Carlo simulations (Methods). The mean and 1σ of the histograms are given. CO_2 concentration leads the global temperature stack in 90% of the simulations and lags it in 6%.

Although other mechanisms contributed to climate change during the ice ages, climate models suggest that their impacts were regional and thus cannot explain the global extent of temperature changes documented by our stacked record alone[9,16,17]. This conclusion is supported by the distinct differences, relative to the temperature stack, in the temporal variabilities of other likely climate change agents (Fig. 3). For example, insolation is a smoothly varying sinusoid that is in antiphase between the hemispheres and sums to near zero globally at the top of the atmosphere (Fig. 3f). Although spatial and temporal asymmetries in albedo could convert insolation to a non-zero forcing at Earth's surface, it is unlikely to account for much of the step-like structure and global nature of the temperature stack.

Similarly, although ice-sheet extent and its associated albedo (from ice cover and emergent continental shelves) and orographic forcing decreased through the deglaciation, global ice volume and area changed only slowly or not at all during intervals of pronounced global warming such as the Oldest Dryas and Younger Dryas, and the greatest volume or area loss in fact occurred during intervals of little or no warming around 19 kyr ago and the Bølling–Allerød (Fig. 3a, b). This distinction is particularly notable during the early Holocene, when the temperature stack had reached interglacial levels while nearly one-third of the excess global ice still remained, although we note that any ice-driven warming would have been partly offset by decreasing greenhouse gas forcing (Fig. 3c and Supplementary Fig. 29a). The apparently small influence of ice-sheet forcing on the temperature stack is consistent with general circulation models that suggest its effect was largely confined to the northern mid to high latitudes and was otherwise modest in the areas sampled by our proxy network[16–18], which is biased away from the ice sheets. Our results, therefore, do not preclude an important contribution to global mean warming from ice-sheet retreat, but suggest that much of this warming was spatially restricted and may be inherently under-represented owing to the lack of suitable palaeotemperature records from and proximal to areas formerly covered by ice.

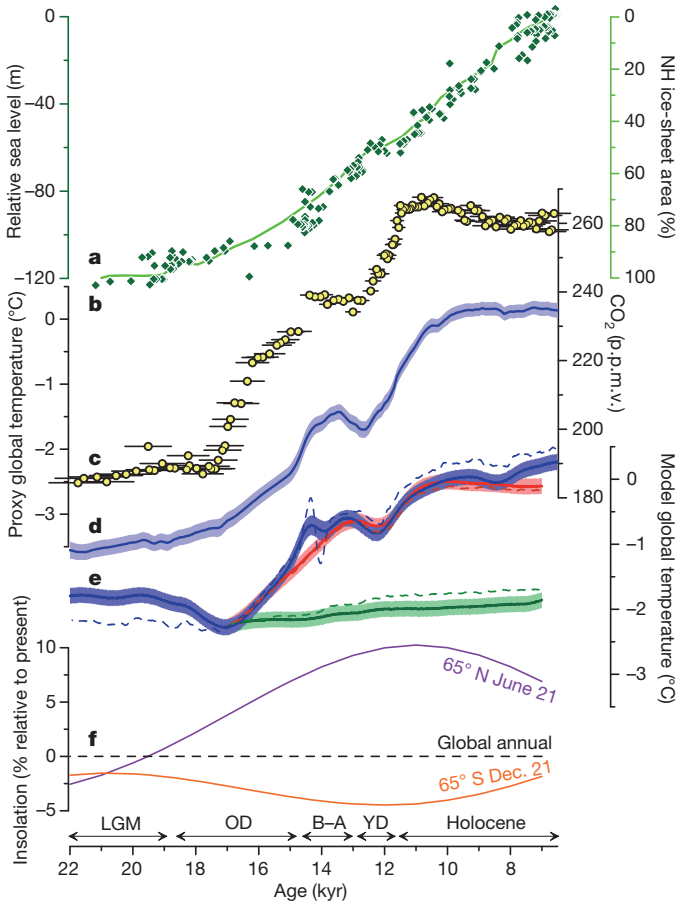

Figure 3 | Global temperature and climate forcings. **a**, Relative sea level[26] (diamonds). **b**, Northern Hemisphere ice-sheet area (line) derived from summing the extents of the Laurentide[43], Cordilleran[43] and Scandinavian (R. Gyllencreutz and J. Mangerud, personal communication) ice sheets through time. **c**, Atmospheric CO_2 concentration. **d**, Global proxy temperature stack. **e**, Modelled global temperature stacks from the ALL (blue), CO2 (red) and ORB (green) simulations. Dashed lines show global mean temperatures in the simulations, using sea surface temperatures over ocean and surface air temperatures over land. **f**, Insolation forcing for latitudes 65° N (purple) and 65° S (orange) at the local summer solstice, and global mean annual insolation (dashed black)[44]. Error bars, 1σ.

Unlike these regional-scale forcings, methane, nitrous oxide and possibly dust are global in nature. Because greenhouse gas forcing was dominated by CO_2 (ref. 19; Supplementary Fig. 29a), and because at the onsets of the Bølling–Allerød, Younger Dryas and Holocene the methane and nitrous oxide records have small step changes like those of the global temperature stack, including these greenhouse gases leaves the correlation with the stack essentially unchanged ($r^2 = 0.93$) and slightly decreases the temperature lag (250 ± 340 yr) (Supplementary Fig. 29). Global dust forcing is poorly constrained[19], however, and we cannot dismiss it as a potentially important driver of global temperature independent of greenhouse warming. Vegetation forcing is likewise difficult to assess[19] and may have significantly contributed to global warming. These uncertainties notwithstanding, we suggest that the increase in CO_2 concentration before that of global temperature is consistent with CO_2 acting as a primary driver of global warming, although its continuing increase is presumably a feedback from changes in other aspects of the climate system.

The global temperature lag behind CO_2 identified here relies critically on the chronological accuracy of these records. The largest uncertainty in the proxy age models is associated with radiocarbon reservoir corrections, which affect marine, but generally not terrestrial, records. A recent synthesis found similar temperature variabilities in land and ocean proxy records during the last deglaciation, but that the timing may be slightly earlier in the marine records[20] (Supplementary Fig. 4). Likewise, the pattern of temperature changes at upwelling sites, where reservoir ages may be more variable, is similar to that at non-upwelling sites but again seems somewhat older (Supplementary Fig. 4). These relationships imply that marine reservoir corrections may have been underestimated, which would shift the temperature stack to later times in some intervals and increase its average lag relative to CO_2. We also evaluated the EPICA Dome C CO_2 chronology[13] by comparing the Dome C methane record on this timescale with the more precisely dated Greenland composite methane record on the GICC05 timescale[21]. This comparison suggests that the EPICA Dome C CO_2 age model may be one to two centuries too young during parts of the deglaciation (Supplementary Fig. 7), which would further increase the lead of CO_2 over global temperature. We thus regard the lag of global temperature behind CO_2 reported here as conservative.

Hemispheric temperatures

The lead of Antarctic temperature over global temperature indicates spatial variability in the pattern of deglacial warming. To examine this spatial variability further, we calculated separate temperature stacks for the Northern Hemisphere and Southern Hemisphere and found that the magnitude of deglacial warming in the two hemispheric stacks is nearly identical (Fig. 4b). Given that greater LGM cooling probably occurred in the areas affected by the Northern Hemisphere ice sheets[9,17], this result provides additional support for our inference that the proxy network under-represents the regional impact of the ice sheets. Each hemispheric stack also shows a two-step warming as seen in the global stack and the CO_2 record (Fig. 4a). Otherwise, the hemispheric stacks differ in two main ways. First, lag correlations suggest that whereas Southern Hemisphere temperature probably leads CO_2, consistent with the Antarctic ice-core results[12], Northern Hemisphere temperature lags CO_2 (Fig. 2b). Second, the Northern Hemisphere shows modest coolings coincident with the onset of Southern Hemisphere warmings, and the warming steps are concave-up in the north but are concave-down in the south (Fig. 4b).

Calculating the temperature difference, ΔT, between the two hemispheric stacks yields an estimate of the heat distribution between the hemispheres, and reveals two large millennial-scale oscillations that are one-quarter to one-third of the glacial–interglacial range in global temperature (Fig. 4d). We attribute the variability in ΔT to variations in the strength of the AMOC and its attendant effects on cross-equatorial heat transport[22,23]. A strong correlation of ΔT with a kinematic proxy (Pa/Th, the protactinium/thorium ratio) for the strength of the AMOC[24] ($r^2 = 0.79$, $P = 0.03$) supports this interpretation (Fig. 4g). We find that ΔT decreases during the Oldest Dryas and Younger Dryas intervals, when the Pa/Th record suggests that the AMOC is weak and heat transfer between the hemispheres is reduced, and that ΔT increases during the LGM, the Bølling–Allerød and the Holocene, when the AMOC is stronger and transports heat from the south to the north. Recalculating ΔT for Atlantic-only records yields the same relations, but they are more pronounced and better correlated with Pa/Th ($r^2 = 0.86$, $P = 0.01$), as would be expected given the importance of the AMOC in this ocean (Fig. 4d). We note that this seesawing of heat between the hemispheres explains the contrast between the lead of Antarctic temperature over CO_2 and the lag of global (and Northern Hemisphere) temperature behind CO_2.

Transient modelling

We evaluate potential physical explanations for the correlations between temperature, CO_2 concentration and AMOC variability in three transient simulations of the last deglaciation using the Community Climate System Model version 3 (CCSM3; ref. 25) of the US National Center for Atmospheric Research. The first simulation (ALL) runs from 22 to 6.5 kyr ago and is driven by changes in greenhouse gases, insolation, ice sheets and freshwater fluxes (the last of which is adjusted iteratively

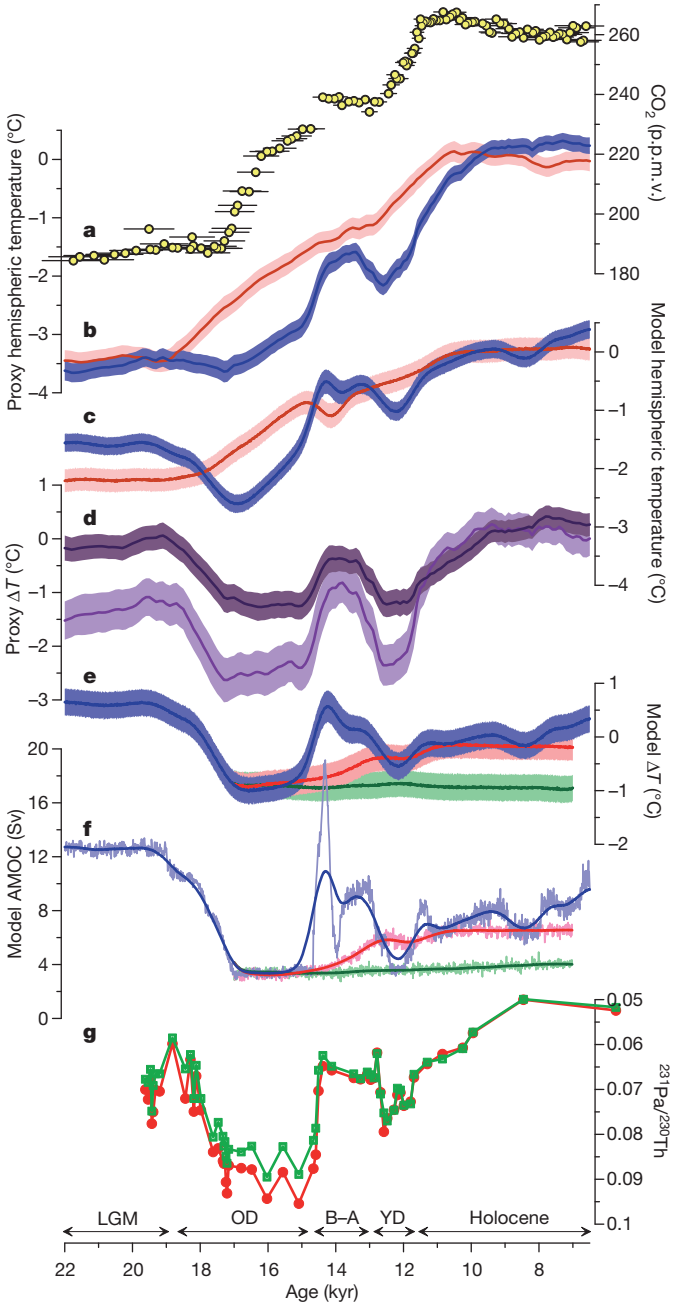

Figure 4 | Hemispheric temperatures. **a**, Atmospheric CO_2 concentration. **b**, Northern Hemisphere (blue) and Southern Hemisphere (red) proxy temperature stacks. **c**, Modelled Northern Hemisphere (blue) and Southern Hemisphere (red) temperature stacks from the ALL simulation. **d**, Northern Hemisphere minus Southern Hemisphere proxy temperature stacks (dark purple). North Atlantic minus South Atlantic region proxy temperature stacks (light purple). **e**, Modelled Northern Hemisphere minus Southern Hemisphere temperature stacks in the ALL (blue), CO2 (red) and ORB (green) simulations. **f**, Modelled AMOC strength in the ALL (blue), CO2 (red) and ORB (green) simulations. **g**, North Atlantic sediment core OCE326-GGC5 $^{231}Pa/^{230}Th$ (ref. 24). Temperatures are given as deviations from the early Holocene (11.5–6.5 kyr ago) mean. Error bars, 1σ.

and thus is a tunable parameter). The second simulation (CO2) is forced only by imposed changes in greenhouse gases (CO_2, methane and nitrous oxide), and the third simulation (ORB) is forced only by orbitally driven insolation variations. All other forcing factors for the second and third simulations, which run from 17 to 7 kyr ago, are held constant at their values at 17 kyr ago. All three simulations include dynamic vegetation feedback and a fixed annual cycle of aerosol forcing. We sample the model output at the locations of the 80 proxy records, recording sea surface temperatures for the marine records and surface air temperatures for the land records, and stacking these sampled model time series just as we did the data. We also correct sea surface temperature time series from the ALL simulation for sea-level changes by scaling the eustatic sea-level curve[26] to a warming by 0.32 °C at the LGM lowstand[27]. To simulate uncertainties in the model results comparable to those of the data, we generated 1,000 Monte Carlo simulations in which the modelled time series were perturbed with random age-model (±300 yr, 1σ) and temperature (±1 °C, 1σ) errors at each site.

The ALL model temperature stack from the 80 sites is similar to the global mean temperature from the model ($r^2 = 0.97$), suggesting that the proxy sites represent the globe fairly well, although the amplitude of warming is slightly smaller in the stack (Fig. 3e and Supplementary Fig. 12). The ALL model stack is also similar to the CO2 model stack in shape and amplitude ($r^2 = 0.98$; Fig. 3e). Because the CO2 model stack reflects a response to only greenhouse gas forcing, its similarity to the ALL stack suggests that greenhouse gases can explain most of the mean warming at these 80 sites. The ORB model stack, by contrast, shows only minor warming, consistent with a modest role for orbital forcing in directly driving global temperature changes.

Calculating the difference in model temperature between the Northern Hemisphere and the Southern Hemisphere at the proxy sites in the three simulations yields ΔT time series that are strongly correlated with variations in modelled AMOC strength in each simulation ($r^2 = 0.95$ for ALL, 0.98 for CO2; Fig. 4f). Only ΔT for the ALL simulation, however, shows millennial-scale variability similar to that seen in the proxy ΔT time series and the Pa/Th record (Fig. 4d, e, g). These results suggest that ocean circulation changes driven primarily by freshwater flux, rather than by direct forcing from greenhouse gases or orbits, are plausible causes of the hemispheric differences in temperature change seen in the proxy records. Furthermore, in the ALL simulation the Southern Hemisphere temperature stack leads Northern Hemisphere (and global) temperature during the two deglacial warming steps (Fig. 4c), supporting our inference that AMOC-driven internal heat redistributions explain the Antarctic temperature lead and global temperature lag relative to CO_2. Lag correlations from 20–10 kyr ago suggest that the modelled global temperature lags CO_2 concentration by 120 yr, which is within the uncertainty range of the proxy-based lag.

The trigger for deglacial warming

The proxy database provides an opportunity to explore what triggers deglacial warming. Substantial temperature change at all latitudes (Fig. 5b), as well as a net global warming of about 0.3 °C (Fig. 2a), precedes the initial increase in CO_2 concentration at 17.5 kyr ago, suggesting that CO_2 did not initiate deglacial warming. This early global warming occurs in two phases: a gradual increase between 21.5 and 19 kyr ago followed by a somewhat steeper increase between 19 and 17.5 kyr ago (Fig. 2a). The first increase is associated with mean warming of the northern mid to high latitudes, most prominently in Greenland, as there is little change occurring elsewhere at this time (Fig. 5 and Supplementary Fig. 20). The second increase occurs during a pronounced interhemispheric seesaw event (Fig. 5), presumably related to a reduction in AMOC strength, as seen in the Pa/Th record and our modelling (Fig. 4f, g). Tropical and Southern Hemisphere warming seem to have more than offset northern extratropical cooling, however, perhaps as a result of an asymmetry in the response of feedbacks such as Southern Ocean sea ice or tropical water vapour, leading to the global mean response. Alternatively, this non-zero-sum response may reflect proxy biases, as tropical warming is not equally evident in all proxies (Supplementary Fig. 20). In any event, we suggest that these spatiotemporal patterns of temperature change are consistent with warming at northern mid to high latitudes, leading to a reduction in the AMOC at ~19 kyr ago, being the trigger for the

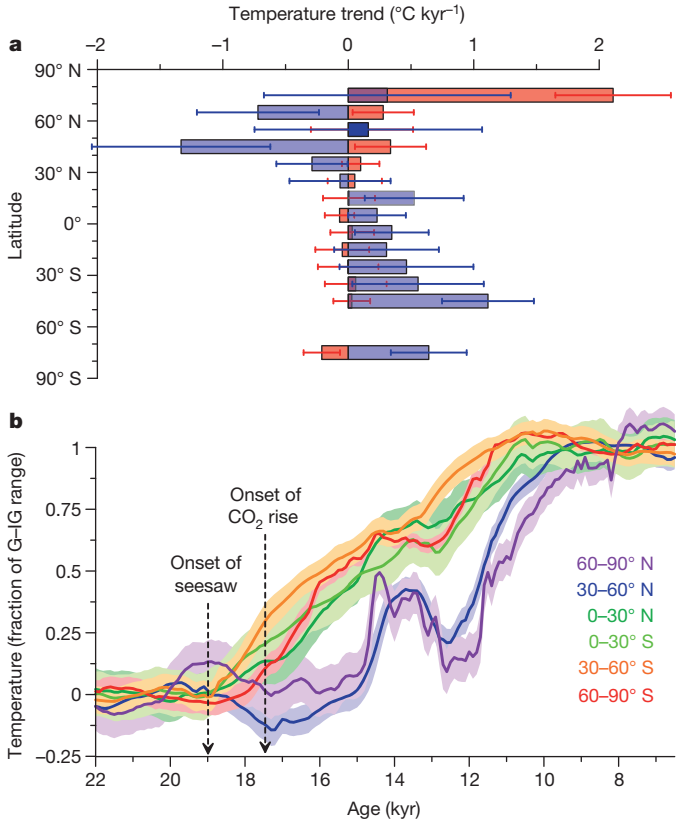

Figure 5 | Temperature change before increase in CO_2 concentration. **a**, Linear temperature trends in the proxy records from 21.5–19 kyr ago (red) and 19–17.5 kyr ago (blue) averaged in 10° latitude bins with 1σ uncertainties. **b**, Proxy temperature stacks for 30° latitude bands with 1σ uncertainties. The stacks have been normalized by the glacial–interglacial (G–IG) range in each time series to facilitate comparison.

global deglacial warming that followed, although more records will be required to confirm the extent and magnitude of early warming at such latitudes. A possible forcing model to explain this sequence of events starts with rising boreal summer insolation driving northern warming[28]. This leads to the observed retreat of Northern Hemisphere ice sheets[26] and the increase in sea level[29] commencing ~19 kyr ago (Fig. 3a, b), with the attendant freshwater forcing causing a reduction in the AMOC that warms the Southern Hemisphere through the bipolar seesaw[30].

Recent studies of the deglaciation[31,32] have shown a strong correlation between times of minima in the AMOC and maxima in CO_2 release, consistent with our ΔT proxy for AMOC strength (Fig. 4d), suggesting that a change in the AMOC may have also contributed to CO_2 degassing from the deep Southern Ocean though its influence on the extent of Southern Ocean sea ice[33], the position of the southern westerlies[34] or the efficiency of the biological pump[35]. Further insight into this relationship is provided by meridional differences in the timing of proxy temperature change following the reduction in AMOC after ~19 kyr ago. A near-synchronous seesaw response is seen from the high northern latitudes to the mid southern latitudes, whereas strong Antarctic warming and the increase in CO_2 concentration lag the AMOC change[36] (Figs 2a and 5b). This lag suggests that the high-southern-latitude temperature response to an AMOC perturbation may involve a time constant such as that from Southern Ocean thermal inertia[23,37], whereas the CO_2 response requires a threshold in AMOC reduction to displace southern winds or sea ice sufficiently[38] or to perturb the ocean's biological pump[35]. We also suggest that the delay of Antarctic warming that follows the AMOC seesaw event 19 kyr ago and occurs relative to the mid southern latitudes over the entire deglaciation (Fig. 5b) is difficult to reconcile with hypotheses invoking a southern high-latitude trigger for deglaciation[39,40].

Our global temperature stack and transient modelling point to CO_2 as a key mechanism of global warming during the last deglaciation. Furthermore, our results support an interhemispheric seesawing of heat related to AMOC variability and suggest that these internal heat redistributions explain the lead of Antarctic temperature over CO_2 while global temperature was in phase with or slightly lagged CO_2. Lastly, the global proxy database suggests that parts of the northern mid to high latitudes were the first to warm after the LGM, which could have initiated the reduction in the AMOC that may have ultimately caused the increase in CO_2 concentration.

METHODS SUMMARY

The data set compiled in this study contains most published high-resolution (median resolution, 200 yr), well-dated ($n = 636$ radiocarbon dates) temperature records from the last deglaciation (see Supplementary Information for the full database). Sixty-seven records are from the ocean and are interpreted to reflect sea surface temperatures, and the remaining 13 record air or lake temperatures on land. All records span 18–11 kyr ago and ~85% of them span 22–6.5 kyr ago. We recalibrated all radiocarbon dates with the IntCal04 calibration (Supplementary Information) and converted proxy units to temperature using the reservoir corrections and proxy calibrations suggested in the original publications. An exception to this was the alkenone records, which were recalibrated with a global core-top calibration[41]. The data were projected onto a $5° \times 5°$ grid, linearly interpolated to 100-yr resolution and combined as area-weighted averages. We used Monte Carlo simulations to quantify pooled uncertainties in the age models and proxy temperatures, although we do not account for analytical uncertainties or uncertainties related to lack of global coverage and spatial bias in the data set. In particular, the records are strongly biased towards ocean margins where high sedimentation rates facilitate the development of high-resolution records. Given these issues, we focus on the temporal evolution of temperature through the deglaciation rather than on its amplitude of change. The global temperature stack is not particularly sensitive to interpolation resolution, areal weighting, the number of proxy records, radiocarbon calibration, infilling of missing data or proxy type. Details on the experimental design of the transient model simulations can be found in ref. 25. The temperature stacks and proxy data set are available in Supplementary Information.

Full Methods and any associated references are available in the online version of the paper at www.nature.com/nature.

Received 16 September 2011; accepted 1 February 2012.

1. Hays, J. D., Imbrie, J. & Shackleton, N. J. Variations in the Earth's orbit: pacemaker of the ice ages. *Science* **194,** 1121–1132 (1976).
2. Delmas, R. J., Ascencio, J. M. & Legrand, M. Polar ice evidence that atmospheric CO_2 20,000 yr BP was 50% of present. *Nature* **284,** 155–157 (1980).
3. Neftel, A., Oeschger, H., Schwander, J., Stauffer, B. & Zumbrunn, R. Ice core sample measurements give atmospheric CO_2 content during the past 40,000 yr. *Nature* **295,** 220–223 (1982).
4. Lüthi, D. *et al.* High-resolution carbon dioxide concentration record 650,000–800,000 years before present. *Nature* **453,** 379–382 (2008).
5. Shackleton, N. J. The 100,000 year ice-age cycle identified and found to lag temperature, carbon dioxide and orbital eccentricity. *Science* **289,** 1897–1902 (2000).
6. Imbrie, J. *et al.* On the structure and origin of major glaciation cycles. 2. The 100,000-year cycle. *Paleoceanography* **8,** 699–735 (1993).
7. Alley, R. B. & Clark, P. U. The deglaciation of the northern hemisphere: a global perspective. *Annu. Rev. Earth Planet. Sci.* **27,** 149–182 (1999).
8. Toggweiler, J. R. & Lea, D. W. Temperature differences between the hemispheres and ice age climate variability. *Paleoceanography* **25,** PA2212 (2010).
9. Weaver, A. J., Eby, M., Fanning, A. F. & Wiebe, E. C. Simulated influence of carbon dioxide, orbital forcing and ice sheets on the climate of the Last Glacial Maximum. *Nature* **394,** 847–853 (1998).
10. Schneider von Deimling, T., Held, H., Ganopolski, A. & Rahmstorf, S. Climate sensitivity estimated from ensemble simulations of glacial climate. *Clim. Dyn.* **27,** 149–163 (2006).
11. Mix, A. C., Ruddiman, W. F. & McIntyre, A. Late Quaternary paleoceanography of the tropical Atlantic, 1: spatial variability of annual mean sea-surface temperatures, 0–20,000 years B.P. *Paleoceanography* **1,** 43–66 (1986).
12. Monnin, E. *et al.* Atmospheric CO_2 concentrations over the last glacial termination. *Science* **291,** 112–114 (2001).
13. Lemieux-Dudon, B. *et al.* Consistent dating for Antarctic and Greenland ice cores. *Quat. Sci. Rev.* **29,** 8–20 (2010).

14. Fischer, H., Wahlen, M., Smith, J., Mastroianni, D. & Deck, B. Ice core records of atmospheric CO_2 around the last three glacial terminations. *Science* **283,** 1712–1714 (1999).
15. Hansen, J. *et al.* Climate response times: dependence on climate sensitivity and ocean mixing. *Science* **229,** 857–859 (1985).
16. Manabe, S. & Broccoli, A. J. The influence of continental ice sheets on the climate of an ice age. *J. Geophys. Res.* **90,** 2167–2190 (1985).
17. Broccoli, A. J. Tropical cooling at the Last Glacial Maximum: an atmosphere-mixed layer ocean model simulation. *J. Clim.* **13,** 951–976 (2000).
18. Chiang, J. C. H. & Bitz, C. M. Influence of high latitude ice cover on the marine Intertropical Convergence Zone. *Clim. Dyn.* **25,** 477–496 (2005).
19. Jansen, E. *et al.* in *Climate Change 2007: The Physical Science Basis* (eds Solomon, S. *et al.*) 433–497 (Cambridge Univ. Press, 2007).
20. Clark, P. U. *et al.* Global climate evolution during the last deglaciation. *Proc. Natl Acad. Sci. USA* advance online publication doi:10.1073/pnas.1116619109 (13 February 2012).
21. Blunier, T. *et al.* Synchronization of ice core records via atmospheric gases. *Clim. Past* **3,** 325–330 (2007).
22. Crowley, T. J. North Atlantic Deep Water cools the Southern Hemisphere. *Paleoceanography* **7,** 489–497 (1992).
23. Stocker, T. F. & Johnsen, S. J. A minimum thermodynamic model for the bipolar seesaw. *Paleoceanography* **18,** 1087 (2003).
24. McManus, J. F., Francois, R., Gherardi, J.-M., Keigwin, L. D. & Brown-Leger, S. Collapse and rapid resumption of Atlantic meridional circulation linked to deglacial climate changes. *Nature* **428,** 834–837 (2004).
25. Liu, Z. *et al.* Transient simulation of last deglaciation with a new mechanism for Bølling-Allerød warming. *Science* **325,** 310–314 (2009).
26. Clark, P. U. *et al.* The Last Glacial Maximum. *Science* **325,** 710–714 (2009).
27. Schmittner, A. *et al.* Climate sensitivity estimated from temperature reconstructions of the Last Glacial Maximum. *Science* **334,** 1385–1388 (2011).
28. Alley, R. B., Brook, E. J. & Anandakrishnan, S. A northern lead in the orbital band: north-south phasing of Ice-Age events. *Quat. Sci. Rev.* **21,** 431–441 (2002).
29. Yokoyama, Y., Lambeck, K., De Deckker, P., Johnston, P. & Fifield, L. K. Timing of the Last Glacial Maximum from observed sea-level minima. *Nature* **406,** 713–716 (2000).
30. Clark, P. U., McCabe, A. M., Mix, A. C. & Weaver, A. J. Rapid rise of sea level 19,000 years ago and its global implications. *Science* **304,** 1141–1144 (2004).
31. Marchitto, T. M., Lehman, S. J., Ortiz, J. D., Fluckiger, J. & van Geen, A. Marine radiocarbon evidence for the mechanism of deglacial atmospheric CO_2 rise. *Science* **316,** 1456–1459 (2007).
32. Skinner, L. C., Fallon, S., Waelbroeck, C., Michel, E. & Barker, S. Ventilation of the deep Southern Ocean and deglacial CO_2 rise. *Science* **328,** 1147–1151 (2010).
33. Stephens, B. B. & Keeling, R. F. The influence of Antarctic sea ice on glacial-interglacial CO_2 variations. *Nature* **404,** 171–174 (2000).
34. Toggweiler, J. R., Russell, J. L. & Carson, S. R. Midlatitude westerlies, atmospheric CO2, and climate change during the ice ages. *Paleoceanography* **21,** PA2005 (2006).
35. Schmittner, A. & Galbraith, E. D. Glacial greenhouse-gas fluctuations controlled by ocean circulation changes. *Nature* **456,** 373–376 (2008).
36. Barker, S. *et al.* Interhemispheric Atlantic seesaw response during the last deglaciation. *Nature* **457,** 1097–1102 (2009).
37. Schmittner, A., Saenko, O. & Weaver, A. J. Coupling of the hemispheres in observations and simulations of glacial climate change. *Quat. Sci. Rev.* **22,** 659–671 (2003).
38. Anderson, R. F. *et al.* Wind-driven upwelling in the Southern Ocean and the deglacial rise in atmospheric CO_2. *Science* **323,** 1443–1448 (2009).
39. Stott, L., Timmermann, A. & Thunell, R. Southern hemisphere and deep-sea warming led deglacial atmospheric CO_2 rise and tropical warming. *Science* **318,** 435–438 (2007).
40. Huybers, P. & Denton, G. Antarctic temperature at orbital timescales controlled by local summer duration. *Nature Geosci.* **1,** 787–792 (2008).
41. Müller, P. J., Kirst, G., Ruhland, G., von Storch, I. & Rosell-Mele, A. Calibration of the alkenone paleotemperature index $U_{37}^{K'}$ based on core-tops from the eastern South Atlantic and the global ocean (60°N-60°S). *Geochim. Cosmochim. Acta* **62,** 1757–1772 (1998).
42. Pedro, J. B. *et al.* The last deglaciation: timing the bipolar seesaw. *Clim. Past Discuss.* **7,** 397–430 (2011).
43. Dyke, A. S. in *Quaternary Glaciations: Extent and Chronology* Vol. 2b (eds Ehlers, J. & Gibbard, P. L.) 373–424 (Elsevier, 2004).
44. Laskar, J. *et al.* A long term numerical solution for the insolation quantities of the Earth. *Astron. Astrophys.* **428,** 261–285 (2004).

Supplementary Information is linked to the online version of the paper at www.nature.com/nature.

Acknowledgements Discussions with numerous people, including E. J. Brook, A. E. Carlson, N. G. Pisias and J. Shaman, contributed to this research. We acknowledge the palaeoclimate community for generating the proxy data sets used here. In particular, we thank S. Barker, T. Barrows, E. Calvo, J. Kaiser, A. Koutavas, Y. Kubota, V. Peck, C. Pelejero, J.-R. Petit, J. Sachs, E. Schefuß, J. Tierney and G. Wei for providing proxy data, and R. Gyllencreutz and J. Mangerud for providing unpublished results of the DATED Project on the retreat history of the Eurasian ice sheets. The NOAA NGDC and PANGAEA databases were also essential to this work. This research used resources of the Oak Ridge Leadership Computing Facility, located in the National Center for Computational Sciences at Oak Ridge National Laboratory, which is supported by the Office of Science of the Department of Energy under contract no. DE-AC05-00OR22725. NCAR is sponsored by the NSF. J.D.S. is supported by a NOAA Climate and Global Change Postdoctoral Fellowship. This research was supported by the NSF Paleoclimate Program for the Paleovar Project through grant AGS-0602395.

Author Contributions J.D.S. designed the study, synthesized and analysed data, and wrote the manuscript with P.U.C. F.H., Z.L. and B.O.-B. did the transient modelling. S.A.M. and A.C.M. contributed to data analysis. A.S. helped interpret AMOC–CO_2 linkages. E.B. provided data and discussion on the radiocarbon calibration. All authors discussed the results and provided input on the manuscript.

Author Information Reprints and permissions information is available at www.nature.com/reprints. The authors declare no competing financial interests. Readers are welcome to comment on the online version of this article at www.nature.com/nature. Correspondence and requests for materials should be addressed to J.D.S. (shakun@fas.harvard.edu).

METHODS

Age control. All radiocarbon dates were recalibrated using Calib 6.0.1 with the IntCal04 calibration and the reservoir corrections suggested in the original publications. Age models based on tuning were left unchanged from the original publications. We used the GICC05 timescale for NGRIP and GRIP, the timescale of ref. 13 for EDML and Dome C, and glaciological age models for the Dome F and Vostok ice cores.

Proxy temperatures. We converted proxy units to temperature for all alkenone, Mg/Ca and TEX_{86} records using the calibrations suggested by the original authors for Mg/Ca and TEX_{86} and the global core-top calibration for alkenone records[41]. We used the published temperature reconstructions for Antarctic ice-core, pollen, microfossil assemblage and MBT/CBT records and the GISP2 borehole calibration for the Greenland ice cores[45]. Missing data values near the beginning and end of the ~15% of records not spanning the entire study interval were infilled using the method of regularized expectation maximization[46].

Stacking. The proxy data were projected onto a $5^\circ \times 5^\circ$ grid, linearly interpolated to 100-yr resolution and combined as area-weighted averages. We do not otherwise account for spatial biases in the dataset or lack of global coverage.

Uncertainty analysis. There are two main sources of uncertainty in the proxy records: age models and temperature calibration. We used a Monte Carlo approach to generate 1,000 realizations of each proxy temperature record after perturbing the records with chronological and temperature errors. These perturbed records were then averaged to yield 1,000 realizations of the global and hemispheric temperature stacks. The error bars on the temperature stacks represent the standard deviations of these 1,000 realizations, which provide an estimate of the propagated uncertainty due to uncertainties in the individual proxy records. A similar approach was applied to the transient model output to develop the modelled temperature stacks and error bars. We developed continuous uncertainty estimates for radiocarbon-based chronologies, taking into account radiocarbon date errors as well as interpolation uncertainty between dates using a random walk model[47]. Age-model uncertainties for tuned records, the Dome F and Vostok ice cores, and regional temperature reconstructions for Beringia[48] were assumed to be 2% (1σ). We used the Dome C and EDML ice-core age-model uncertainties[13] and GICC05 maximum counting errors[49,50] as 2σ uncertainties for the NGRIP and GRIP ice cores as suggested in ref. 50. We used the following 1σ temperature calibration uncertainties: alkenones, $T = (U^{K'}_{37} - 0.044 \pm 0.016)/(0.033 \pm 0.001)$ (ref. 41); Mg/Ca $= \pm 0.02B\exp(\pm 0.003AT)$, where A and B are constants (ref. 51); TEX_{86}, $\pm 1.7\,^\circ$C (ref. 52); ice cores, $\pm 10\%$ (ref. 53); pollen, microfossil assemblages and MBT/CBT, $\pm 1.5\,^\circ$C. We did not account for analytical uncertainties in proxy measurements. Chronological errors in the Monte Carlo simulations were temporally autocorrelated but were random in space (but this does not account for systematic errors among the proxy records due to uncertainties in the radiocarbon calibration), whereas temperature errors were assumed to be random in space and time. We note that our study is concerned with temperature anomalies and is thus sensitive to relative but not absolute temperature errors in a proxy record. See Supplementary Information for more details and examples. Age-model uncertainties for the Antarctic Dome C CO_2 record related to methane synchronization to Greenland were estimated on the basis of the combined uncertainties associated with Greenland layer counting, Greenland ice-age/gas-age differences and methane tuning to Antarctica. These uncertainties were used to generate 1,000 realizations of the CO_2 record, which together with the 1,000 temperature stack realizations yield the 1,000 temperature–concentration lead–lag estimates shown in Fig. 2b.

Robustness of results. We evaluated how well the proxy sites represent the globe by subsampling the twentieth-century instrumental temperature record and our transient modelling output of the deglaciation at the 80 proxy sites. Both approaches suggested that the mean of the proxy sites approximates the global mean fairly well. We recalculated the stack after interpolating the records to 500-yr resolution but this did not change the time series or its uncertainty. Differences in areal weighting affect the glacial–interglacial amplitude of the stack but have little impact on its structure. Jackknifing suggests that the stack is not particularly sensitive to the number of records used. A leave-one-out proxy jackknifing approach suggests that the correlation ($r^2 = 0.90$–0.95) and lead–lag relation (300–600-yr temperature lag) between global temperature and CO_2 concentration are not sensitive to proxy type. Statistical infilling of missing data values has negligible impact on the results. Although we here use the IntCal04 radiocarbon calibration, we tested the sensitivity of our results to this choice by recalibrating radiocarbon dates using the IntCal09 calibration. This makes the global stack up to 350 yr older during the Heinrich 1 interval, and shifts the overall phase lag relative to CO_2 concentration from 460 ± 340 to 350 ± 340 yr. We consider the IntCal04 calibration to be more accurate for the reasons discussed in Supplementary Information. Lag correlations suggest that Antarctic temperature led CO_2 concentration slightly throughout the deglaciation, whereas global temperature led CO_2 concentration at the onset of deglaciation but lagged behind it thereafter. The lead–lag relation between CO_2 concentration and the global temperature stack is not significantly changed by detrending the time series to remove the deglacial ramp in each quantity. The significance levels of the correlations between global temperature and CO_2 concentration and between Pa/Th and ΔT were determined by calculating effective sample sizes of these highly autocorrelated time series (CO_2 concentration, 4.3; global temperature, 4.1; Pa/Th, 5.4; ΔT, 6.2; Atlantic ΔT, 5.5) using equation 6.26 of ref. 54. See Supplementary Information for more discussion of these tests.

Model freshwater forcing. Whereas the forcing from insolation, greenhouse gases and ice sheets during the deglaciation are fairly well constrained, freshwater forcing is comparatively uncertain. Several model freshwater schemes were tested, and the final run was based on the meltwater scenario (Supplementary Fig. 30) that produced North Atlantic climate variability in best agreement with proxy reconstructions. The raw modelled AMOC time series (Fig. 4f, thin lines) were effectively smoothed with a Monte Carlo approach similar to the one used to develop the modelled temperature stacks (Fig. 4e), to facilitate direct comparison of the two. More specifically, the smoothed AMOC time series (Fig. 4f, bold lines) are the means of 1,000 realizations of the raw AMOC time series generated by perturbing them with 300-yr (1σ) age-model errors.

45. Cuffey, K. M. & Clow, G. D. Temperature, accumulation, and ice sheet elevation in central Greenland through the last deglacial transition. *J. Geophys. Res.* **102,** 26383–26396 (1997).
46. Schneider, T. Analysis of incomplete climate data: estimation of mean values and covariance matrices and imputation of missing values. *J. Clim.* **14,** 853–871 (2001).
47. Huybers, P. & Wunsch, C. A depth-derived Pleistocene age model: uncertainty estimates, sedimentation variability, and nonlinear climate change. *Paleoceanography* **19,** PA1028 (2004).
48. Viau, A. E., Gajewski, K., Sawada, M. C. & Bunbury, J. Low- and high-frequency climate variability in eastern Beringia during the past 25 000 years. *Can. J. Earth Sci.* **45,** 1435–1453 (2008).
49. Rasmussen, S. O. *et al.* Synchronization of the NGRIP, GRIP, and GISP2 ice cores across MIS 2 and palaeoclimatic implications. *Quat. Sci. Rev.* **27,** 18–28 (2008).
50. Svensson, A. *et al.* A 60000 year Greenland stratigraphic ice core chronology. *Clim. Past* **4,** 47–57 (2008).
51. Anand, P., Elderfield, H. & Conte, M. H. Calibration of Mg/Ca thermometry in planktonic foraminifera from a sediment trap time series. *Paleoceanography* **18,** 1050 (2003).
52. Kim, J. H., Schouten, S., Hopmans, E. C., Donner, B. & Damste, J. S. S. Global sediment core-top calibration of the TEX_{86} paleothermometer in the ocean. *Geochim. Cosmochim. Acta* **72,** 1154–1173 (2008).
53. Jouzel, J. *et al.* Magnitude of isotope/temperature scaling for interpretation of central Antarctic ice cores. *J. Geophys. Res.* **108,** 4361 (2003).
54. von Storch, H. & Zwiers, F. W. *Statistical Analysis in Climate Research* 115 (Cambridge Univ. Press, 1999).

SUPPLEMENTARY INFORMATION

doi:10.1038/nature10915

Contents:

1. Proxy database

2. Age control

3. Monte Carlo simulations

4. How well do proxy sites represent the globe?

5. How robust is the temperature stack?

6. CO_2-temperature relationship

7. Model freshwater forcing

8. Comparison with Schmittner et al. (2011)

Appendix S1. Proxy age models

Appendix S2. Proxy temperature records

1. Proxy database

1.1 Database

The database used in this study is composed of 80 published high-resolution temperature records derived from alkenones (n=32), planktic foraminiferal Mg/Ca (n=26), microfossil assemblages (n=6), ice-core stable isotopes (n=6), pollen (n=4), TEX_{86} (n=4), and MBT/CBT (n=2) (Table S1). Only records of reasonably high resolution (generally < 500 years) and firm chronological control (generally ≥ 4 radiocarbon dates) were included. Sixty-seven records are dated by radiocarbon, six are ice cores dated by layer counting and/or glaciological modeling, four are dated by a combination of radiocarbon and tuning to layer-counted records, two are entirely tuned to other radiometric chronologies, and one is dated by biostratigraphy.

Table S1. The deglacial proxy temperature database used in this study.

#	Location	Core	Proxy	Reference	Lat (°)	Lon (°)	Elev/Depth (m)	Chronology	Resolution (yr)
1	NGRIP, Greenland	-	ice core $\delta^{18}O$ and borehole temp	Cuffey and Clow, 1997[1]; Andersen et al., 2006[2], Rasmussen et al., 2006[3]	75.1	-42.3	2917	layer counted	20
2	GRIP, Greenland	-	ice core $\delta^{18}O$ and borehole temp	Cuffey and Clow, 1997[1]; Rasmussen et al., 2006[3], 2007[4]	72.6	-37.6	3200	layer counted	20
3	Burial Lake, Alaska	-	chironomids	Kurek et al., 2009[5]	68.4	-159.2	460	^{14}C	352
4	Eastern Beringia (A)	-	pollen	Viau et al., 2008[6]	67.5	-165	-	^{14}C	101
5	Eastern Beringia (B)	-	pollen	Viau et al., 2008[6]	67.5	-137.5	-	^{14}C	101
6	Eastern Beringia (C)	-	pollen	Viau et al., 2008[6]	62.5	-165	-	^{14}C	124
7	Eastern Beringia (D)	-	pollen	Viau et al., 2008[6]	62.5	-137.5	-	^{14}C	101
8	Northeast Atlantic	NA 87-22	foram assemblages	Waelbroeck et al., 2001[7]	55.5	-14.7	-2161	^{14}C and SST tuned to Greenland	246
9	Northeast Atlantic	MD01-2461	Mg/Ca	Peck et al., 2008[8]	51.8	-12.9	-1153	^{14}C and N. pachyderma (s.) %	116

								tuned to Greenland116	
10	California margin	W8709A-8	$U^{K'}_{37}$	Prahl et al., 1995[9]	42.5	-127.7	-3111	^{14}C	620
11	central North Atlantic	CH 69-09	foram assemblages	Waelbroeck et al., 2001[7]	41.8	-47.4	-4100	^{14}C and SST tuned to Greenland	167
12	Japan margin	PC-6	$U^{K'}_{37}$	Minoshima et al., 2007[10]	40.4	143.5	-2215	^{14}C biostratigraphy (foraminiferal ecozones ^{14}C-dated elsewhere)	167
13	Western Mediterranean	BS79-38	$U^{K'}_{37}$	Cacho et al., 2001[11]	38.4	13.6	-1489		155
14	Iberian margin	SU81-18	$U^{K'}_{37}$	Bard et al., 2000[12]	37.8	-10.2	-3135	^{14}C	316
15	Iberian margin	SU81-18	foram assemblages	Waelbroeck et al., 2001[7]	37.8	-10.2	-3135	^{14}C benthic $\delta^{18}O$ tuned to ^{14}C-dated core SU90/08	234
16	North Atlantic	MD95-2037	$U^{K'}_{37}$	Calvo et al., 2001[13]	37.1	-32.0	-2630		484
17	Gulf of Cadiz	M39-008	$U^{K'}_{37}$	Cacho et al., 2001[11]	36.4	-7.1	-576	^{14}C	113
18	Alboran Sea	MD95-2043	$U^{K'}_{37}$	Cacho et al., 1999[14]	36.1	-2.6	-1841	^{14}C	152
19	North Pacific	MD01-2421	$U^{K'}_{37}$	Isono et al., 2009[15]	36	141.8	-2224	^{14}C loess proxy records tuned to ^{230}Th-dated Hulu/Sanbao Cave speleothems	246
20	Chinese loess plateau	Section MS2008E	MBT/CBT	Peterse et al., 2011[16]	34.9	113.3	~200		397
21	Bermuda Rise	OCE326-GGC5	Mg/Ca	Carlson et al., 2008[17]	33.7	-57.6	-4550	^{14}C	408
22	Japan margin	KT92-17 St. 14	$U^{K'}_{37}$	Sawada and Handa, 1998[18]	32.6	138.6	-3252	^{14}C	443
23	Blake outer ridge	KNR140-51GGC	Mg/Ca	Carlson et al., 2008[17]	32.6	-76.3	-1790	^{14}C	397
24	Nile Delta	GeoB 7702-3	TEX_{86}	Castañeda et al., 2010[19]	31.7	34.1	-562	^{14}C	316
25	Japan margin	KY07-04-01	Mg/Ca	Kubota et al., 2010[20]	31.6	128.9	-758	^{14}C	115
26	East China Sea	MD98-2195	$U^{K'}_{37}$	Ijiri et al., 2005[21]	31.6	129	-746	^{14}C	165
27	Gulf of Mexico	MD02-2575	Mg/Ca	Ziegler et al., 2008[22]	29.0	-87.1	-847	^{14}C	282
28	Red Sea	GeoB 5844-2	$U^{K'}37$	Arz et al., 2003[23]	27.7	34.7	-963	^{14}C	316
29	Gulf of Mexico	EN32-PC6	Mg/Ca	Flower et al., 2004[24]	27.0	-91.3	-2280	^{14}C	185
30	Northwest African margin	ODP 658C	foram assemblages	deMenocal et al., 2000[25]	20.8	-18.6	-2263	^{14}C	176
31	Northwest African margin	ODP 658C	$U^{K'}_{37}$	Zhao et al., 1995[26]	20.8	-18.6	-2263	^{14}C	115
32	South China Sea	17940	$U^{K'}_{37}$	Pelejero et al., 1999[27]	20.1	117.4	-1968	^{14}C	161
33	South China Sea	ODP 1144	Mg/Ca	Wei et al, 2007[28]	20.1	117.6	-2037	^{14}C	337
34	Arabian Sea	74KL	$U^{K'}_{37}$	Huguet et al., 2006[29]	14.3	57.3	-3212	^{14}C	304
35	Arabian Sea	74KL	TEX_{86}	Huguet et al., 2006[29]	14.3	57.3	-3212	^{14}C	310
36	Western tropical North Atlantic	M35003-4	$U^{K'}_{37}$	Rühlemann et al., 1999[30]	12.1	-61.3	-1299	^{14}C	344
37	Western Caribbean Sea	VM28-122	Mg/Ca	Schmidt et al., 2004[31]	11.6	-78.4	-3623	^{14}C	352
38	Arabian Sea	NIOP-905	$U^{K'}_{37}$	Huguet et al., 2006[29]	10.8	51.9	-1567	^{14}C	204
39	Arabian Sea	NIOP-905	TEX_{86}	Huguet et al., 2006[29]	10.8	51.9	-1567	^{14}C	204
40	Cariaco Basin, Venezuala	PL07-39PC	Mg/Ca	Lea et al., 2003[32]	10.7	-65.0	-790	^{14}C and grayscale tuned to varved core 56PC	110
41	Sulu Sea	MD97-2141	Mg/Ca	Rosenthal et al., 2003[33]	8.8	121.3	-3633	^{14}C	78
42	Eastern equatorial Pacific	MD02-2529	$U^{K'}_{37}$	Leduc et al., 2007[34]	8.2	-84.1	-1619	^{14}C	282
43	Eastern equatorial Pacific	ME0005A-43JC	Mg/Ca	Benway et al., 2006[35]	7.9	-83.6	-1368	^{14}C	207
44	South China Sea	MD01-2390	$U^{K'}_{37}$	Steinke et al., 2008[36]	6.6	113.4	-1545	^{14}C	287
45	South China Sea	MD01-2390	Mg/Ca	Steinke et al., 2008[36]	6.6	113.4	-1545	^{14}C	221
46	West Pacific warm pool	MD98-2181	Mg/Ca	Stott et al., 2007[37]	6.3	125.8	-2114	^{14}C	56
47	Gulf of Guinea	MD03-2707	Mg/Ca	Weldeab et al., 2007[38]	2.5	9.4	-1295	^{14}C	90
48	Eastern equatorial Atlantic	GeoB 4905	Mg/Ca	Weldeab et al,. 2005[39]	2.5	9.4	-1328	^{14}C	180
49	Eastern equatorial Pacific	TR163-22	Mg/Ca	Lea et al., 2006[40]	0.5	-92.4	-2830	^{14}C	242
50	Eastern equatorial Pacific	ME0005A-24JC	$U^{K'}_{37}$	Kienast et al., 2006[41]	0.0	-86.5	-2941	^{14}C	209
51	Eastern equatorial Pacific	V21-30	$U^{K'}_{37}$	Koutavas and Sachs, 2008[42]	-1.2	-89.7	-617	^{14}C	360
52	Eastern equatorial Pacific	V21-30	Mg/Ca	Koutavas et al., 2002[43]	-1.2	-89.7	-617	^{14}C	408
53	Eastern equatorial Pacific	V19-28	$U^{K'}_{37}$	Koutavas and Sachs, 2008[42]	-2.4	-84.7	-2720	^{14}C	596
54	Brazilian margin	GeoB 3910	$U^{K'}_{37}$	Jaeschke et al., 2007[44]	-4.2	-36.3	-2362	^{14}C	221
55	Western tropical Atlantic	GeoB 3129	Mg/Ca	Weldeab et al, 2006[45]	-4.6	-36.6	-830	^{14}C	112
56	West Pacific warm pool	MD9821-62	Mg/Ca	Visser et al., 2003[46]	-4.7	117.9	-1855	^{14}C	323
57	West Pacific warm pool	MD98-2176	Mg/Ca	Stott et al., 2007[37]	-5.0	133.4	-2382	^{14}C	119

58	Gulf of Guinea	GeoB 6518-1	MBT/CBT	Weijers et al., 2007[47]	-5.6	11.2	-962	^{14}C	189
59	Gulf of Guinea	GeoB 6518-1	$U^{K'}_{37}$	Schefuß et al., 2005[48]	-5.6	11.2	-962	^{14}C	204
60	Lake Tanganyika	NP04-KH3, KH4	TEX_{86}	Tierney et al., 2008[49]	-6.7	29.6	773	^{14}C	221
61	West Pacific warm pool	MD98-2165	Mg/Ca	Levi et al., 2007[50]	-9.7	118.4	-2100	^{14}C	176
62	West Pacific warm pool	MD98-2170	Mg/Ca	Stott et al., 2007[37]	-10.6	125.4	-832	^{14}C	369
63	Timor Sea, Indian Ocean	MD01-2378	Mg/Ca	Xu et al., 2008[51]	-13.1	121.8	-1783	^{14}C	131
64	Southeast Atlantic	GeoB 1023-5	$U^{K'}_{37}$	Kim et al., 2002[52]	-17.2	11.0	-1978	^{14}C	97
65	Indian Ocean	MD79257	$U^{K'}_{37}$	Bard et al., 1997[53]	-20.4	36.3	-1260	^{14}C	282
66	Subtropical southeast Atlantic	ODP 1084B	Mg/Ca	Farmer et al., 2005[54]	-25.5	13.0	-1992	^{14}C	91
67	Brazilian margin	KNR159-5-36GGC	Mg/Ca	Carlson et al., 2008[17]	-27.5	-46.5	-1268	^{14}C	484
68	Chilean margin	GeoB 7139-2	$U^{K'}_{37}$	Kaiser et al., 2005[55]	-30.2	-72.0	-3270	^{14}C	330
69	South Australia	MD03-2611	$U^{K'}_{37}$	Calvo et al., 2007[56]	-36.7	136.7	-2420	^{14}C	344
70	New Zealand	MD97-2121	$U^{K'}_{37}$	Pahnke and Sachs, 2006[57]	-40.4	178.0	-3014	^{14}C	84
71	Chilean margin	ODP 1233	$U^{K'}_{37}$	Lamy et al., 2007[58]	-41.0	-74.5	-838	^{14}C	112
72	Southeast Atlantic	TN057-21-PC2	$U^{K'}_{37}$	Sachs et al., 2001[59]	-41.1	7.8	-4981	^{14}C	110
73	Southeast Atlantic	TN057-21	Mg/Ca	Barker et al., 2009[60]	-41.1	7.8	-4981	^{14}C	168
74	New Zealand	SO136-GC11	$U^{K'}_{37}$	Barrows et al., 2007[61]	-43.5	167.9	-1556	^{14}C	194
75	New Zealand	MD97-2120	$U^{K'}_{37}$	Pahnke and Sachs, 2006[57]	-45.5	174.9	-1210	^{14}C	122
76	Southern Ocean	MD88-770	foram assemblages	Labeyrie et al., 1996[62]	-46.0	96.5	-3290	^{14}C	218
77	EDML, Antarctica	-	ice core $\delta^{18}O$	Stenni et al., 2010[63]; Lemieux-Dudon et al., 2010[64]	-75	0	2892	glaciological model and stratigraphic constraints	103
78	Dome C, Antarctica	-	ice core $\delta^{18}O$	Stenni et al., 2010[63]; Lemieux-Dudon et al., 2010[64]	-75.1	123.4	3240	glaciological model and stratigraphic constraints	103
79	Dome Fuji, Antarctica	-	ice core $\delta^{18}O$, δD	Kawamura et al., 2007[65]	-77.3	39.7	3810	glaciological model	500
80	Vostok, Antarctica	-	ice core δD	Petit et al., 1999[66]	-78.5	108.0	3500	glaciological model	62

1.2 Data density

A total of ~8400 proxy temperature measurements and 636 radiocarbon dates among the 80 records lie within the interval 22-6.5 ka (Figure S1a,b). The median resolution of the records is 200 years (Figure S2). All 80 records span 18-11 ka and ~85% span 22-6.5 ka (Figure S1c).

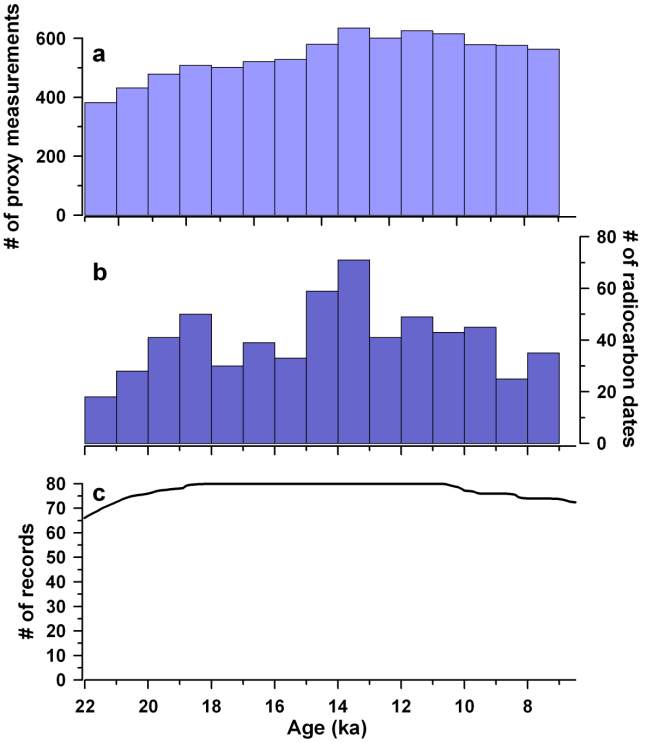

Figure S1: Data density. Distribution of (**a**) proxy temperature measurements, (**b**) radiocarbon dates, and **(c)** proxy records through time.

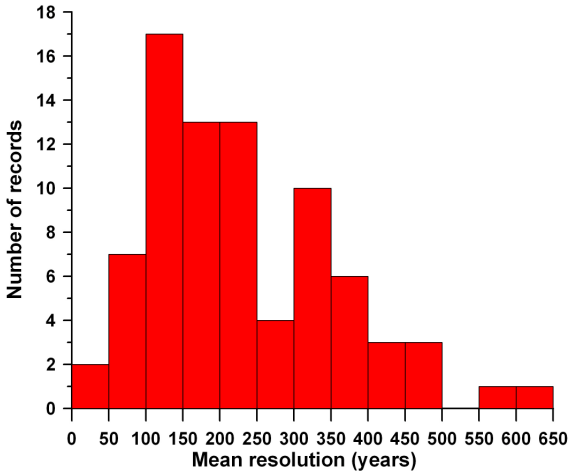

Figure S2: Histogram of the mean resolution of the proxy records from 22-6.5 ka.

2. Age control

The three most common types of age control used in this synthesis are radiocarbon ages, Greenland layer counts, and Antarctic timescales. We discuss each and their uncertainties here.

2.1 Radiocarbon ages

Most of the non-ice core records are either directly or indirectly tied into radiocarbon chronologies. Radiocarbon-based age models have three main sources of uncertainty: (1) marine reservoir correction uncertainties, (2) errors on calibrated radiocarbon dates, and (3) interpolating age models between dates. The latter two were explicitly accounted for in our Monte Carlo simulations.

(1) We applied the reservoir corrections used by the original authors, which average 463 years over the 19-6 ^{14}C ka interval (Figure S3). Reservoir corrections were assumed to be 400 years if not otherwise stated in the original publications. Assuming larger (smaller) reservoir corrections would shift the temperature stack younger (older).

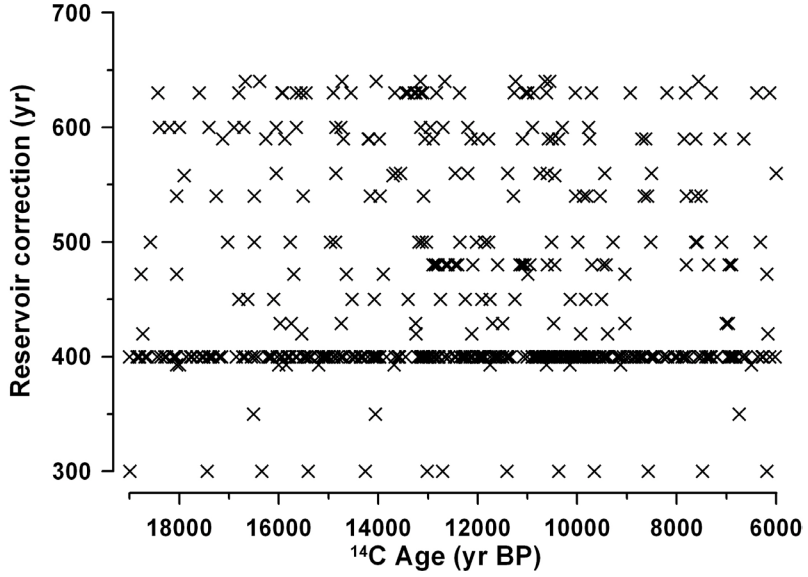

Figure S3: Radiocarbon reservoir corrections for all dates from the 62 radiocarbon-dated marine records in the database, as suggested by the original authors.

One way to check the reasonableness of the applied reservoir corrections is to compare climate signals in marine and terrestrial records, since terrestrial archives generally do not suffer from radiocarbon reservoir issues. Clark et al.[67] recently calculated the two leading modes of deglacial temperature variability from a global proxy dataset using empirical orthogonal function analysis. Dividing the dataset into land (n=53) and ocean (n=74) records yields similar leading modes of variability (r^2=0.98 and 0.80 for principal components 1 and 2), suggesting that the two realms record the same climate signals (Figure S4). Lag correlations suggest the ocean modes are 300 years older than the land modes, however, which may imply reservoir corrections have been underestimated. Similar logic can be applied to upwelling versus non-upwelling regions in the ocean to investigate reservoir corrections, since reservoir ages are expected to be more variable at upwelling sites. The two leading modes of variability for calibrated sea surface temperature records from upwelling (n=19) and non-upwelling (n=50) areas appear to be reversed, such that non-upwelling PC1 correlates with upwelling PC2 (r^2=0.93) and non-upwelling PC2 correlates with upwelling PC1 (r^2=0.81), indicating that the millennial variability mode is more important at upwelling sites while the overall deglacial warming mode dominates at non-upwelling sites (Figure S4). Nonetheless, the strong correlations of these climate modes suggest that the two domains may record the same signals. Lag correlations suggest the upwelling modes are older than the non-upwelling modes by 300 and 200 years, which again may imply underestimated marine reservoir corrections. These observations therefore imply that, if anything, errors in reservoir corrections might shift the global temperature stack slightly younger, increasing its lag behind atmospheric CO_2.

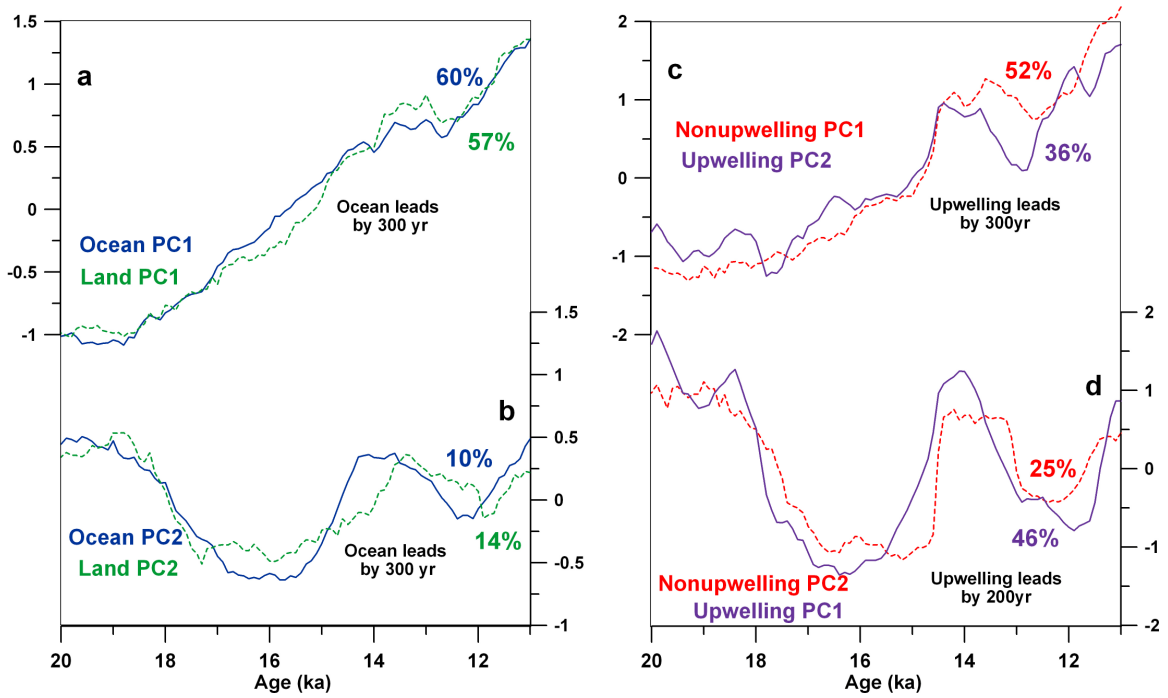

Figure S4: Leading principal components (PC) of deglacial temperatures variability. (**a,b**) land and ocean sites. (**c,d**) upwelling and non-upwelling sites in the ocean. The fraction of variance explained by the modes and their relative timing as determined from lag correlations are given. (adapted from Clark et al.[67])

(2) All dates were recalibrated with Calib 6.0.1 using the IntCal04 calibration. To simplify the often non-Gaussian errors on calibrated radiocarbon dates, we treated the upper and lower 2σ calibrated ages as a Gaussian 2σ uncertainty about a centered mean age in the Monte Carlo simulations. Age models were then allowed to vary within these uncertainties at the depths of the radiocarbon dates.

(3) Between radiocarbon dates, we used a random walk model[68] that allows age models to "jitter" more the further they are from a radiocarbon date. To determine a reasonable jitter value (J) we used the existing radiocarbon dates in the database between 10 and 20 ka and calculated the deviation of a date from its expected (i.e., linear) age between two bounding dates. This procedure was repeated for all possible permutations of dates, yielding 3769 values of J (Figure S5). We used the median J value (J = 188) to

perturb the radiocarbon-based age models with autocorrelated errors in our Monte Carlo analysis. Age models and their estimated uncertainties are shown in Appendix S1.

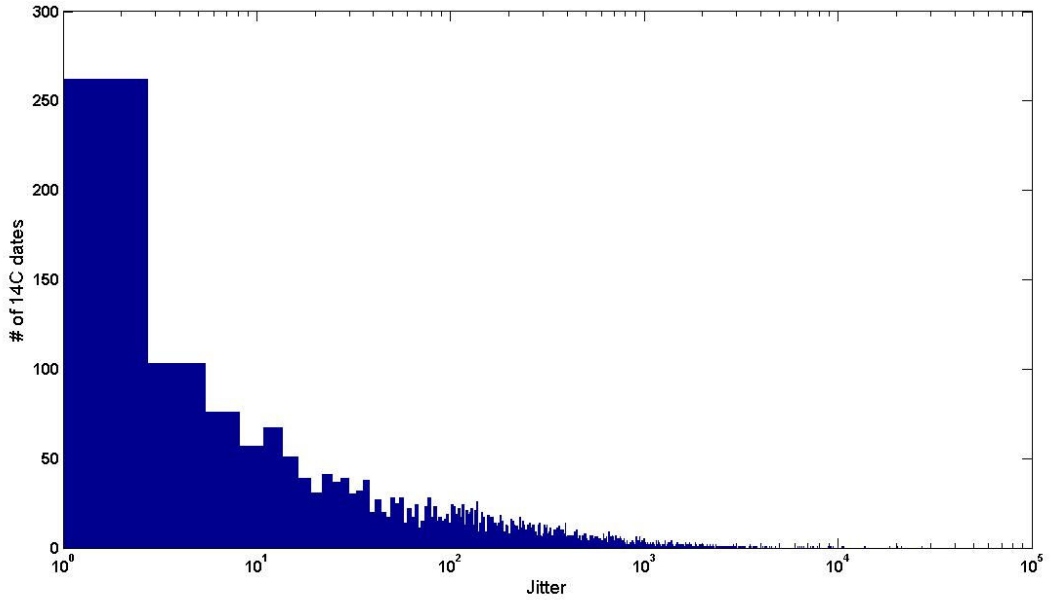

Figure S5: Histogram of 3769 age model jitter values calculated from radiocarbon data from 20-10 ka, as described in the text. The median jitter value is 188.

A final uncertainty related to radiocarbon dating is the calibration, which is discussed below in Section 5.5.

2.2 Greenland layer counting

The NGRIP and GRIP ice cores are anchored by the layer-counted GICC05 timescale, and four other marine records are tuned to earlier layer-counted Greenland timescales. GICC05 appears to be fairly well linked into the radiocarbon timescale during the deglaciation[69]. Maximum counting errors for GICC05 suggest that absolute age uncertainty (1σ) increases from approximately 10 to 265 years over our 6.5-22 ka study interval (≤ 1.2% errors) (refs. 3,70). Our Monte Carlo simulations used these time-varying uncertainties for the NGRIP and GRIP ice cores, and assumed 2% uncertainties for the records tuned to Greenland.

2.3 Antarctic timescales

The EDC and EDML ice cores have been synchronized with Greenland by Lemieux-Dudon et al.[64], and we use their time-varying error estimates, which approach nearly 400 years (2σ) at the onset of deglaciation. Pedro et al.[71] suggest a similar uncertainty for their composite Antarctic record based on five ice cores at the onset of deglaciation. The age models of the Dome F and Vostok ice cores are based on glaciological flow models, and we assume 2% (1σ) errors.

Critical to our analysis is the age model and uncertainty for the atmospheric CO_2 record. We used EDC CO_2, which was recently placed on an improved timescale based on a best compromise between glaciological modeling and ice and gas stratigraphic constraints among several Antarctic and Greenland ice cores by Lemieux-Dudeon et al.[64]. Because Lemieux-Dudon et al.[64] did not quantify gas age uncertainties, however, we estimated chronological uncertainties for the CO_2 record based on the errors associated with CH_4 synchronization of EDC with Greenland. There are three sources of uncertainty in this process that we account for. First, the Greenland ice-age timescale (GICC05) is derived from annual layer counting of the NGRIP ice core. Andersen et al.[70] and Rasmussen et al.[3] provide "maximum counting errors" associated with this process, which Andersen et al. suggest regarding as 2σ uncertainties. Second, transferring the GICC05 ice age timescale to the Greenland composite CH_4 record[72] requires knowledge of Greenland ice age-gas age differences, or delta ages. A rigorous assessment of delta age uncertainty does not exist in the literature. We therefore considered delta age uncertainty to be 20% of delta age itself, an estimate that we regard as conservative. In actuality, delta age is precisely known during the abrupt onsets of the Bølling, Younger

Dryas, and Holocene periods, when nitrogen and argon isotopes indicate CH_4 and Greenland ice $\delta^{18}O$ variations were nearly synchronous[73]. Third, CH_4 concentration errors introduce uncertainty during tuning of EDC CH_4 to the Greenland composite CH_4 record. We estimated this uncertainty with 1000 Monte Carlo simulations in which the two CH_4 records were randomly perturbed with 10 ppbv errors (1σ) and tuned using the program XCM[68]. To provide a conservative estimate of the combined uncertainty due to these three sources of error, we added them arithmetically (Figure S6).

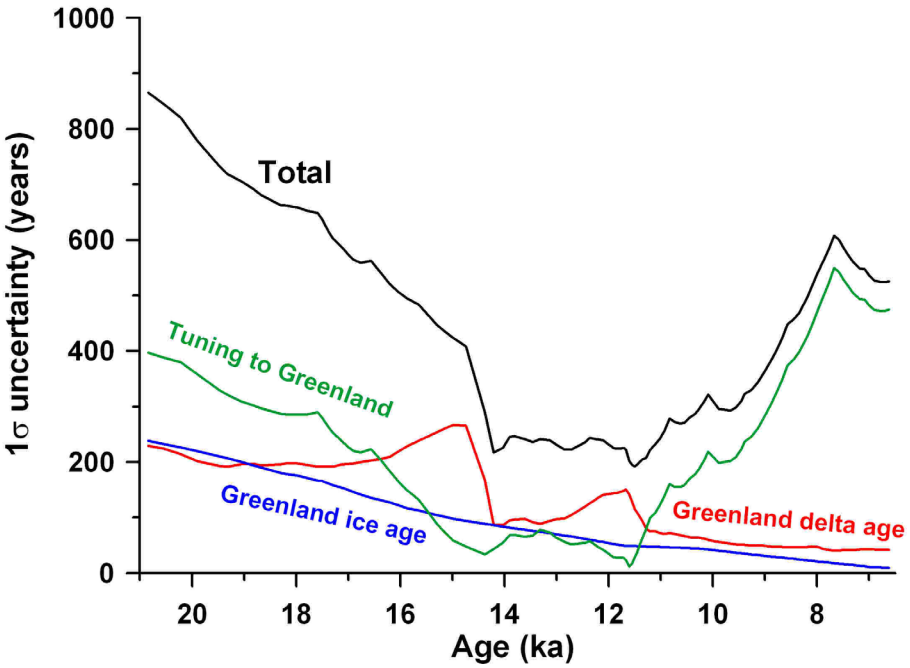

Figure S6: CO_2 age-model uncertainty. Total age uncertainty in the EDC CO_2 record over the last deglaciation associated with methane-synchronization to Greenland (black), which reflects the sum of uncertainties associated with Greenland ice ages (blue), Greenland ice age-gas age differences (red), and tuning EDC and Greenland CH4

To further examine the robustness of the Lemieux-Dudon et al.[64] EDC gas chronology, we compared it to GICC05. EDC CH_4 tuned to GICC05 is generally older than on the Lemieux-Dudon et al.[64] timescale, and this offset is particularly evident at the Bølling onset (Figure S7b). Greenland composite CH_4 and NGRIP $\delta^{18}O$ on Lemieux-

Dudon et al.[64] exhibit a similar offset at the Bølling onset (Figure S7a). Since abrupt Greenland warmings are known to be synchronous with CH_4 jumps[73], this offset likely reflects an error in the Lemieux-Dudon et al.[64] gas chronology, which if corrected would shift the EDC CO_2 record a couple centuries older at the Bølling (Figure S7c). A similar though smaller offset seems to occur at the Younger Dryas while no offset exists at the Holocene onset (Figure S7d). The lack of structure in the CH_4 record at the onset of deglaciation makes it difficult to precisely determine the timing of the initial CO_2 rise, which is reflected in the larger error bars at this time (Figure S6).

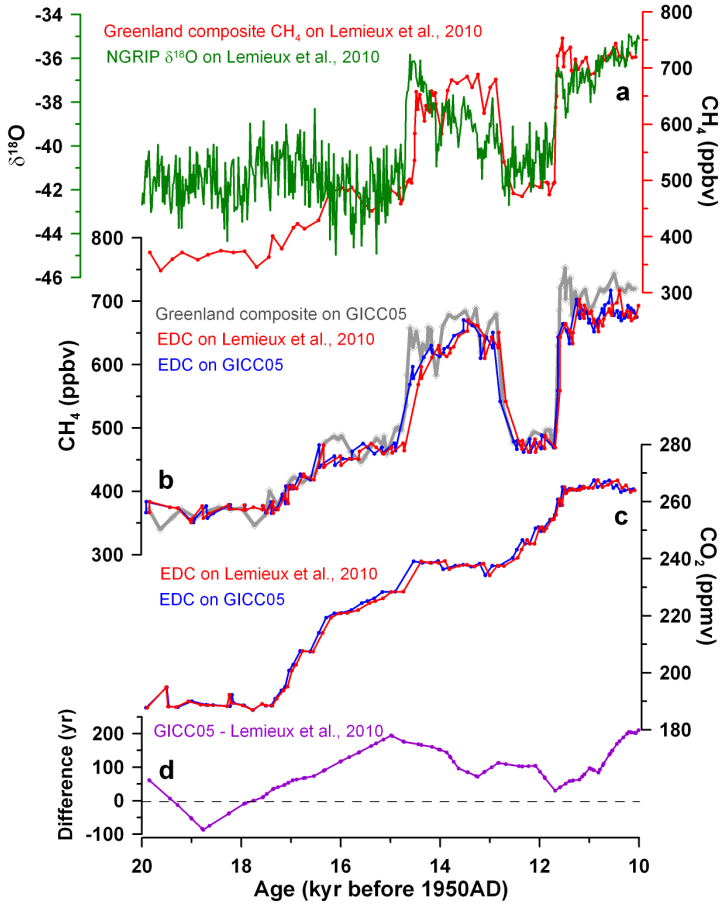

Figure S7: Ice core age models. (**a**) Greenland composite CH_4 and NGRIP $\delta^{18}O$ on the Lemieux-Dudon et al.[64] timescale. (**b**) Greenland composite CH_4 on the GICC05 timescale and EDC CH_4 on the Lemieux-Dudon et al.[64] and GICC05 timescales. (**c**) EDC CO_2 on the Lemieux-Dudon et al.[64] and GICC05 timescales. (**d**) Difference between the Lemieux-Dudon et al.[64] and GICC05 gas timescales.

3. Monte Carlo simulations

We used Monte Carlo simulations to generate 1000 realizations of each proxy temperature record, and the global temperature stack in turn. An example record is shown in Figure S8. First, continuous age-model uncertainty estimates were calculated for each record as explained above in Section 2.1 (Figure S8a). 1000 age models were then generated for each record by perturbing its chronology with autocorrelated errors using these uncertainty estimates (Figure S8b). Age models were linearly extrapolated beyond the top and bottommost dates in a core using the mean sedimentation rate over the dated interval of the core. Next, the proxy values were converted to temperature 1000 times, perturbing the temperature calibration with the errors given in the Methods section of the paper (Figure S8c); temperature errors were assumed to be random in time and space. These perturbed proxy temperature records were then linearly interpolated onto the perturbed age models at 100-year resolution and converted to anomalies from the early Holocene (11.5-6.5 ka) mean to yield 1000 realizations of each record (Figure S8d). Lastly, the first realizations of the 80 records were stacked, followed by the second, third, fourth, etc., generating 1000 realizations of the global temperature stack (Figure S9). The temperature stack and error bars shown in the main paper are the mean and standard deviation of these 1000 realizations. Temperature records and their estimated uncertainties are shown in Appendix S2. The analytical code used in this study will be published in Marcott et al.[74].

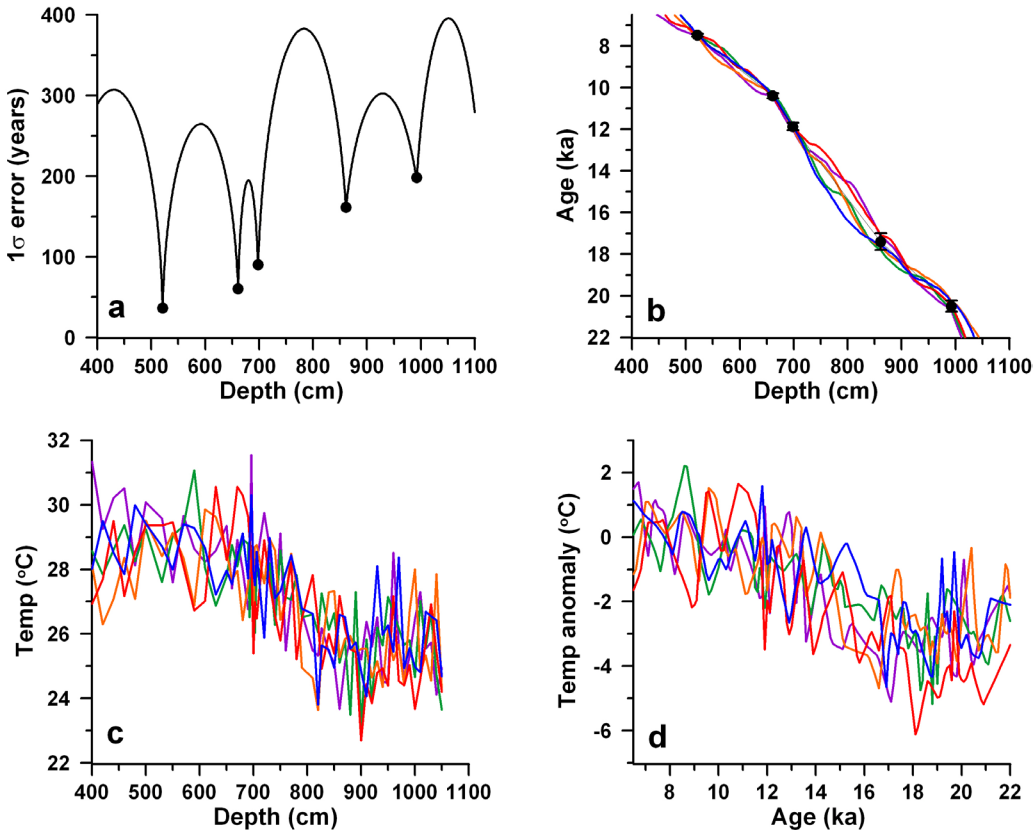

Figure S8: Example of five Monte Carlo simulations with the Visser et al.[46] West Pacific Warm Pool Mg/Ca record. (**a**) Estimated age model error. Black dots show the locations of radiocarbon dates. (**b**) Perturbed age models. Black dots and error bars show radiocarbon dates. (**c**) Perturbed temperature records. (**d**) Perturbed temperature records linearly interpolated onto the perturbed age models at 100-year resolution and referenced as anomalies from the early Holocene (11.5-6.5 ka) mean.

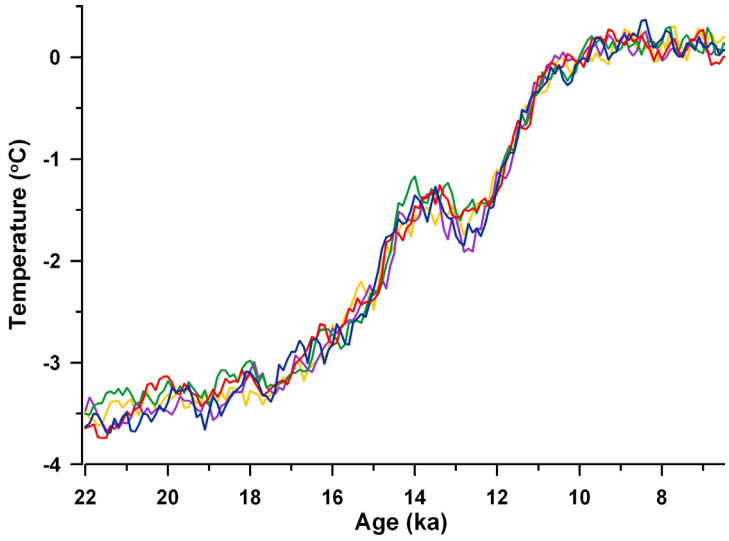

Figure S9: Five realizations of the global temperature stack, derived from perturbing the proxy records with chronological and temperature calibration errors.

The standard deviation of the 1000 global temperature stacks provides a measure of the propagated error due to chronological and temperature uncertainties in the individual records (Figure S10). We performed this Monte Carlo procedure including only temperature uncertainties, only chronological uncertainties, and both temperature and chronological uncertainties. We find that error in the temperature stack due to chronological uncertainties generally increases with age, as expected, though there are local maxima in error at times of large temperature shifts, such as the onsets of the deglaciation, Bølling/Allerød, Younger Dryas, and Holocene. Errors associated with temperature uncertainties are constant through time, as would also be expected. Temperature uncertainties generally contribute substantially more error to the temperature stack than chronological uncertainties. Tests indicate that errors are proportional to $n^{-½}$, where n is the number of proxy records.

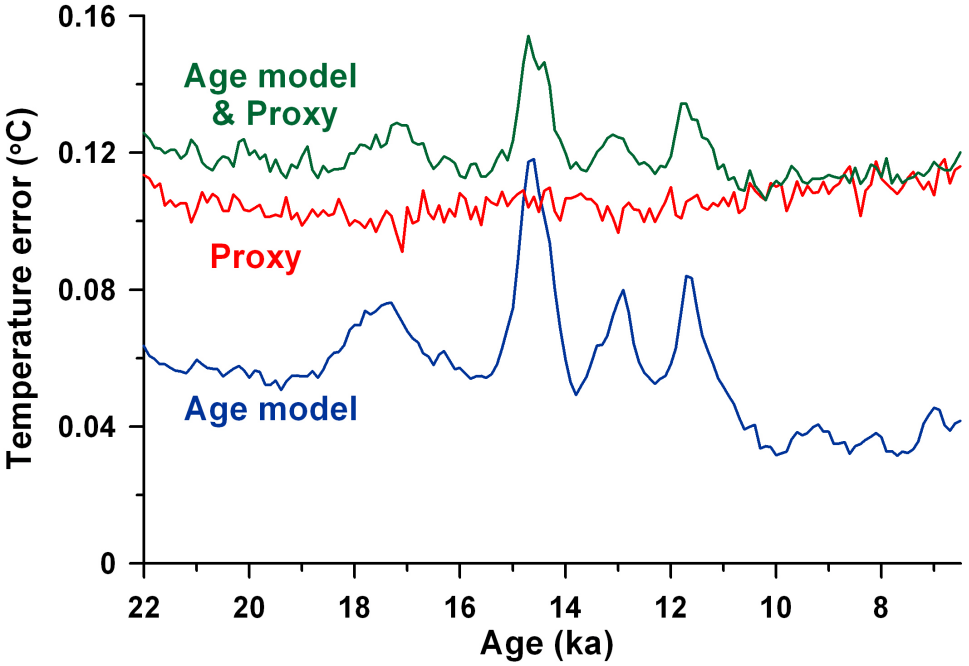

Figure S10: Global temperature stack uncertainties. 1σ error on the global proxy temperature stack due to uncertainties in the age models of the records (blue), the conversion of proxy values to temperature (red), and both (green).

4. How well do the proxy sites represent the globe?

An important assumption of our study is that the 80 proxy records used provide a reasonable representation of global temperature variability. We evaluated this assumption using the instrumental temperature record as well as output from our transient modeling of the last deglaciation.

4.1 Instrumental record

We sampled the 5x5-degree NCDC instrumental blended land and ocean surface temperature dataset from 1880-2007 A.D.[75] at 80 random locations 1000 times to generate 1000 realizations of global mean temperature. The standard deviation of these realizations is 4.5 times smaller than the standard deviation of 20th century global temperature suggesting 80 random points represents the globe reasonably well (Figure S11a). In addition, the mean at the locations of the deglacial proxy records is similar to the true global mean (r^2=0.83), indicating these particular locations faithfully capture the global signal. Repeating this procedure for 67 ocean-only sites (i.e., the number of ocean proxy records) with the 1x1-degree HadISST1 dataset from 1870-2007 A.D.[76] yields similar results (Figure S11b).

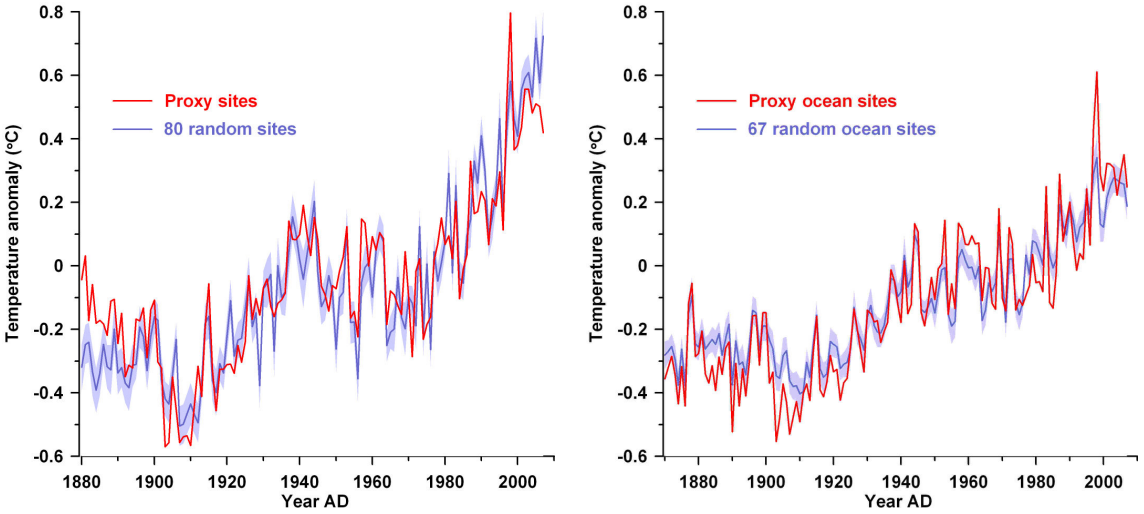

Figure S11: 20th century temperatures at the proxy sites. (a) The mean (blue line) and standard deviation (blue error window) of 1000 realizations of global mean temperature based on a random sampling of 80 locations from the NCDC blended land and ocean dataset (this is equivalent to the true global mean)[75]. Mean temperature at the locations of the 80 deglacial proxy sites (red). **(b)** Same as (a), except confined to the ocean and using the HadISST1 dataset[76].

4.2 Transient deglacial model output

We also compared the mean temperature at the 80 proxy sites in our deglacial model to the global and hemispheric means in the model. The temporal structures of the proxy site means and full-field means are all similar, but while the glacial-interglacial amplitude is accurately represented by the proxy sites in the Southern Hemishere, it is underestimated by ~1°C in the Northern Hemisphere (Figure S12).

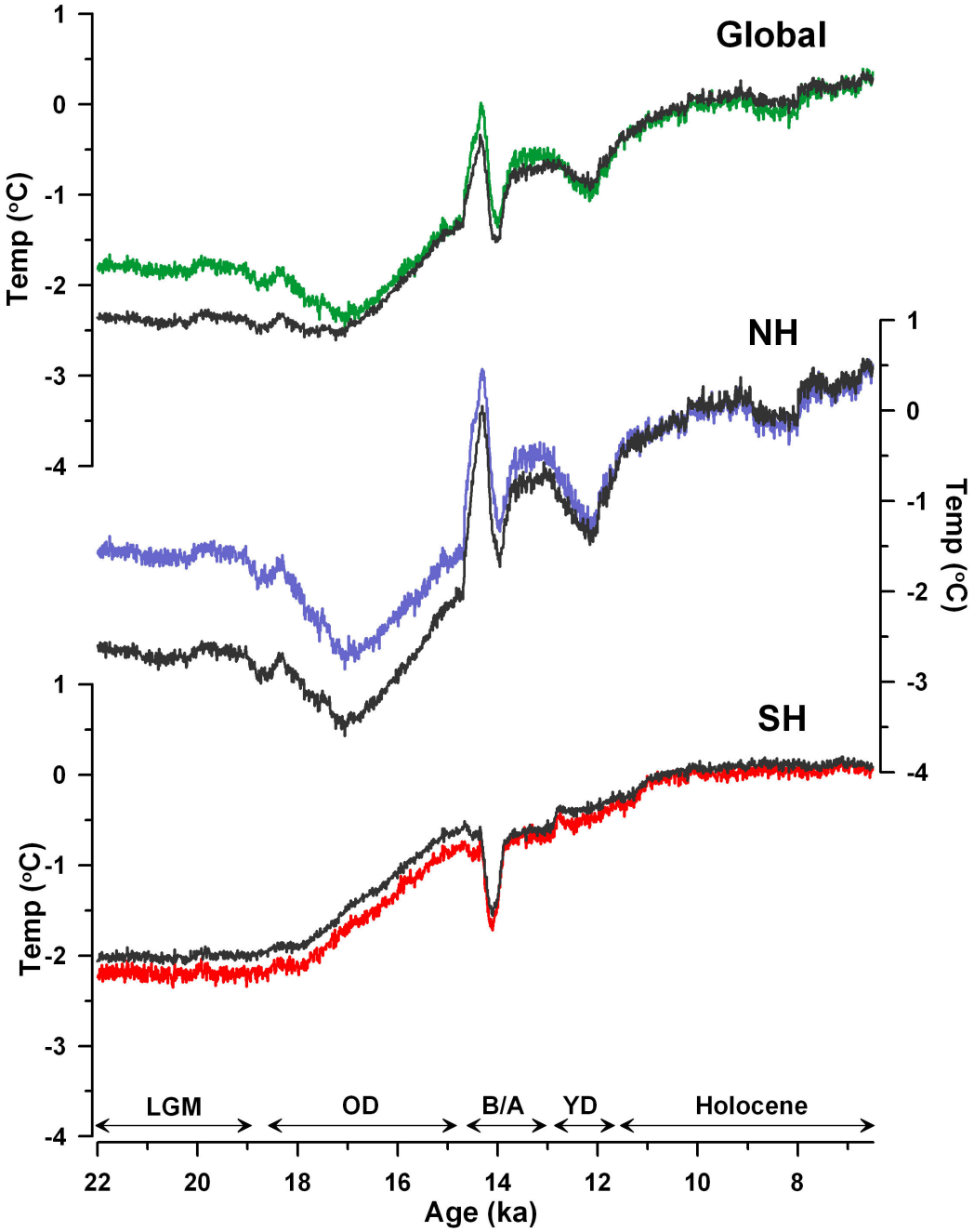

Figure S12: Simulated temperature stacks versus full-field mean temperatures. The mean temperatures in the model for the (**top**) globe, (**middle**) Northern Hemisphere, (**bottom**) and Southern Hemisphere (black), and the area-weighted means in the model at the 80 proxy sites (colored). Sea surface temperatures are used over ocean and surface air temperatures are used over land.

5. How robust is the temperature stack?

We investigate the sensitivity of the proxy temperature stack to several variables including interpolation resolution, areal weighting, the number and type of proxy records, missing data, and radiocarbon calibration.

5.1 Resolution

Recalculating the global temperature stack at 500-year resolution yields an essentially identical stack and error bars, albeit at lower resolution (Figure S13). This is because our uncertainty estimate for global temperature at any given point in time is the standard deviation of 1000 realizations of the global temperature anomaly at that point derived from perturbing the individual records with errors, linearly interpolating to constant resolution, and stacking. So, for example, 500-year resolution results in 1000 global temperature estimates at 11 and 11.5 ka. 100-year resolution yields the exact same results for 11 and 11.5 ka, as well as 1000 temperature estimates at 11.1, 11.2, 11.3, and 11.4 ka that are generally in between those at 11 and 11.5 ka due to the linear interpolation.

We also recalculated the stack using only the records with better than 200-year resolution (n=39; 23 in Northern Hemisphere, 16 in Southern Hemisphere). This stack is, in general, similar, though there is greater overall warming and a larger Younger Dryas cooling (Figure S14).

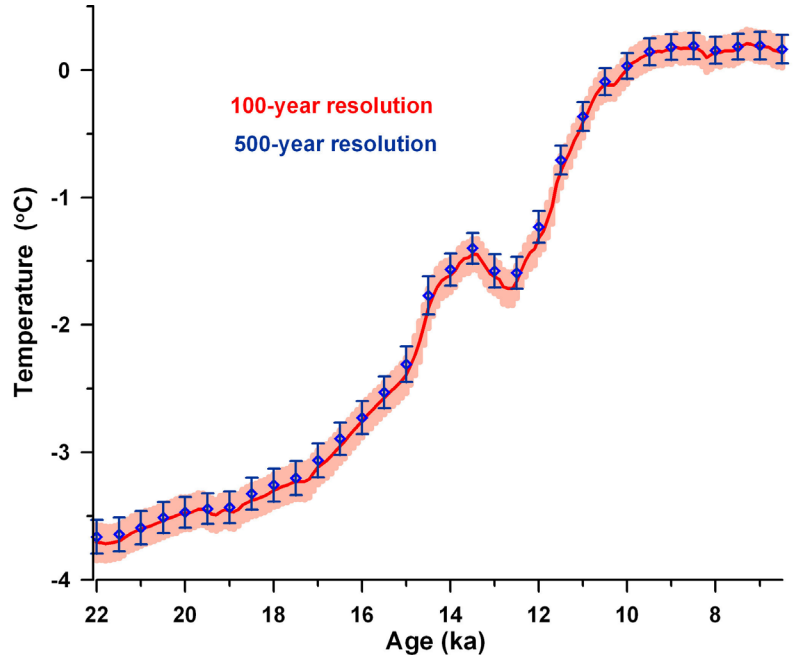

Figure S13: The global temperature stack based on proxy records interpolated to 100-year and 500-year resolution. Errors (1σ) reflect age-model and temperature calibration uncertainty.

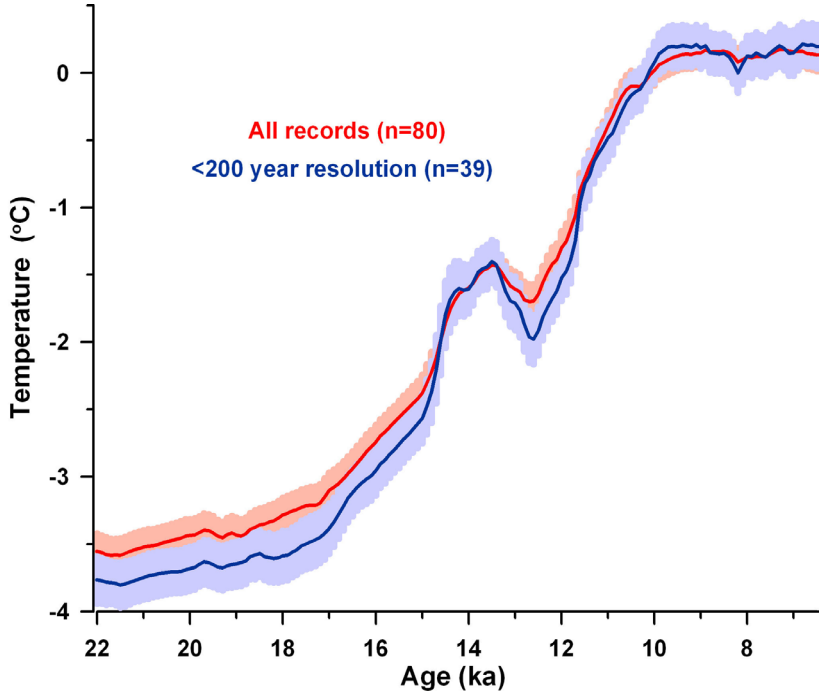

Figure S14: The global temperature stack based on all records and only the records with higher than 200-year resolution. Errors (1σ) reflect age-model and temperature calibration uncertainties.

5.2 Areal weighting

To test the sensitivity of the global temperature stack to areal weighting we show the results of three different schemes here: (1) the area-weighted 5° x 5° gridded average we use in the main paper; (2) the unweighted raw average of the records; (3) a meridional weighting in which the records are first averaged in 10° latitude bands and then stacked weighting by latitude-band area; latitude bands without records were represented by the adjacent latitude band with data. These three stacks have similar temporal structures (Figure S15), suggesting the correlation and phasing of temperature and CO_2 we report is not strongly sensitive to areal weighting. The amplitudes of the stacks differ by up to 15%, however, implying the spatial bias of our dataset affects its ability to constrain the magnitude of glacial cooling.

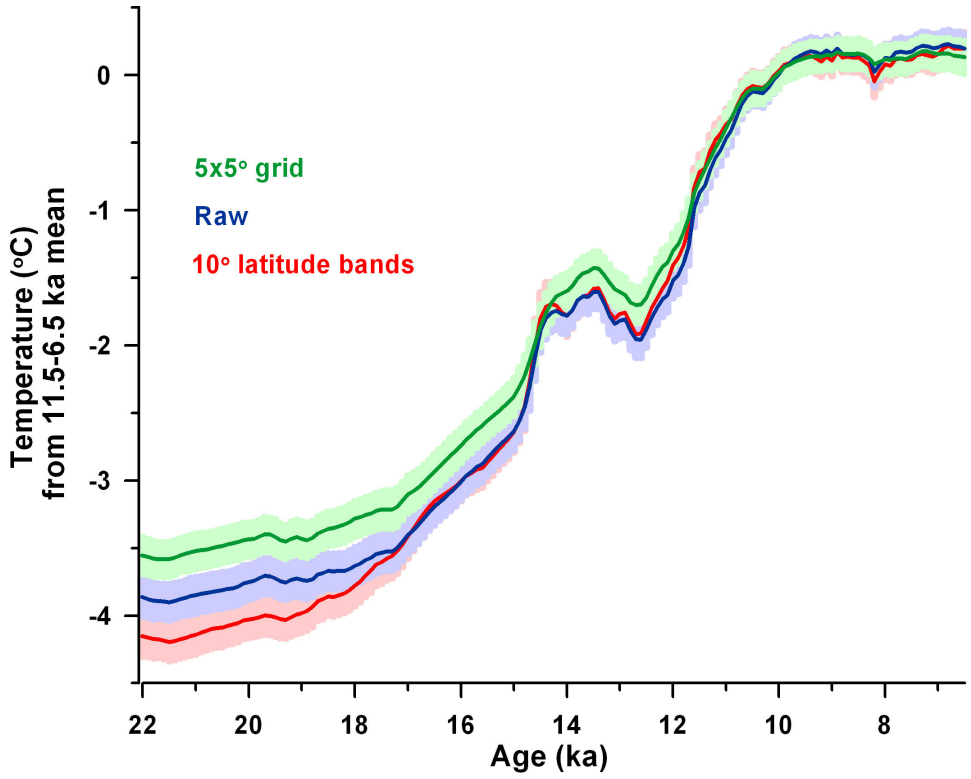

Figure S15: The global temperature stack based on various area-weighting schemes of the data. Errors (1σ) reflect age-model and temperature calibration uncertainties.

5.2 Jackknifing

We used a jackknifing approach to examine the sensitivity of the temperature stack to the number of records used. The stack was recalculated 1000 times after randomly excluding 50% of the records each time. This procedure was also repeated excluding 90% of the records. Note that because the records were perturbed with chronological and proxy errors before jackknifing, the results include these sources of uncertainty. The standard deviation of the jackknifed stacks, particularly for the 50% case, are relatively modest in comparison to the variability in the proxy stack (Figure S16), which suggests the stack is fairly robust and unlikely to change dramatically with the inclusion of more records in the future.

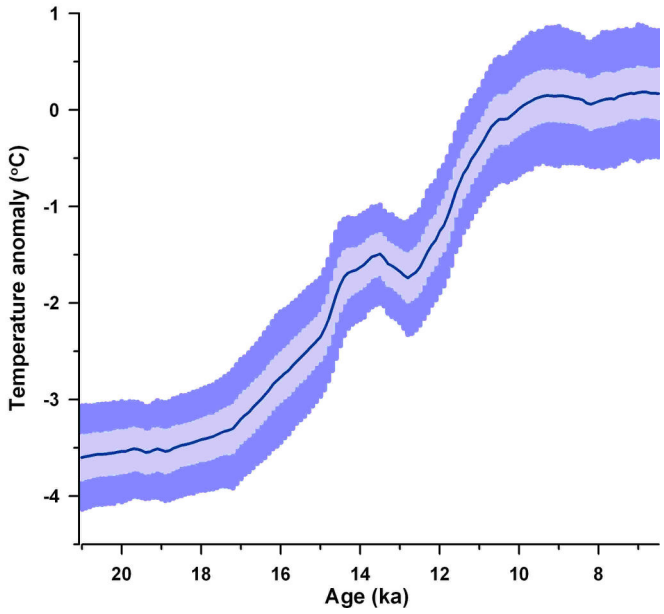

Figure S16: Jackknifed temperature stacks. The unweighted global proxy stack with 1σ error bars derived from 1000 jackknifed stacks randomly excluding 50% (light blue errors) and 90% (dark blue errors) of the records.

5.3 Proxy type

To assess how our temperature reconstructions may be affected by disagreement among the proxies we calculated separate stacks for each proxy type (Figure S17) as well as jackknifed global and hemispheric stacks leaving out one proxy at a time (Figure S18). Differing temperature histories are expected for each proxy type to some extent given the large range in the number and locations of records for each proxy (Figure 1 in the main paper). There is general consistency among the jackknifed global stacks of a two-step deglaciation during the Oldest and Youngest Dryas intervals, with relatively stable temperatures during the Last Glacial Maximum, Bølling/Allerød, and early Holocene. Thus, the correlations between the jackknifed stacks and CO_2 from 22-6.5 ka are all similar ranging from r^2=0.90 to 0.95, as are the temperature lags behind CO_2 based on 20-10 ka lag correlations ranging from 300 to 600 years. The timing of initial warming and the magnitude of the glacial-interglacial change varies among the jackknifed stacks, however. Also, excluding the Mg/Ca records yields a moderate 0.25°C global warming during the early Holocene (Figure S17), which would increase its correlation with ice-sheet retreat and perhaps imply a somewhat larger role for ice-sheet forcing on the temperature stack. We evaluated whether this cooling trend in Mg/Ca is an artifact of an early Holocene peak in carbonate preservation[77] by comparing early Holocene Mg/Ca temperature trends with core depth, since carbonate preservation effects are expected to exert a larger impact on deeper sites. We find little correlation between temperature trend and depth, however, suggesting this early Holocene feature is not an artifact of carbonate preservation (Figure S19).

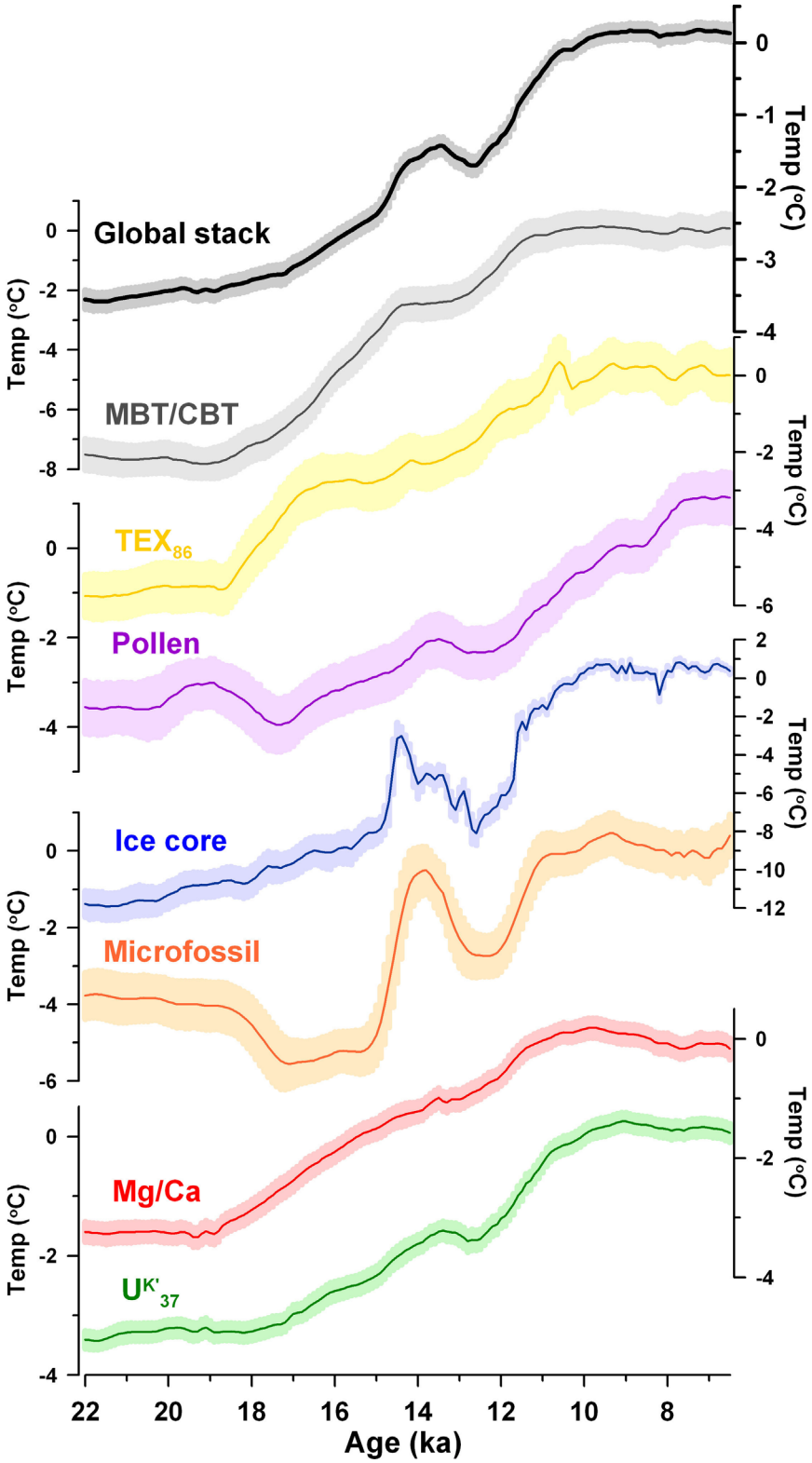

Figure S17: Unweighted temperature stacks by proxy type, with 1σ errors reflecting chronological and temperature calibration uncertainties in the records. The global temperature stack is shown at the top for reference.

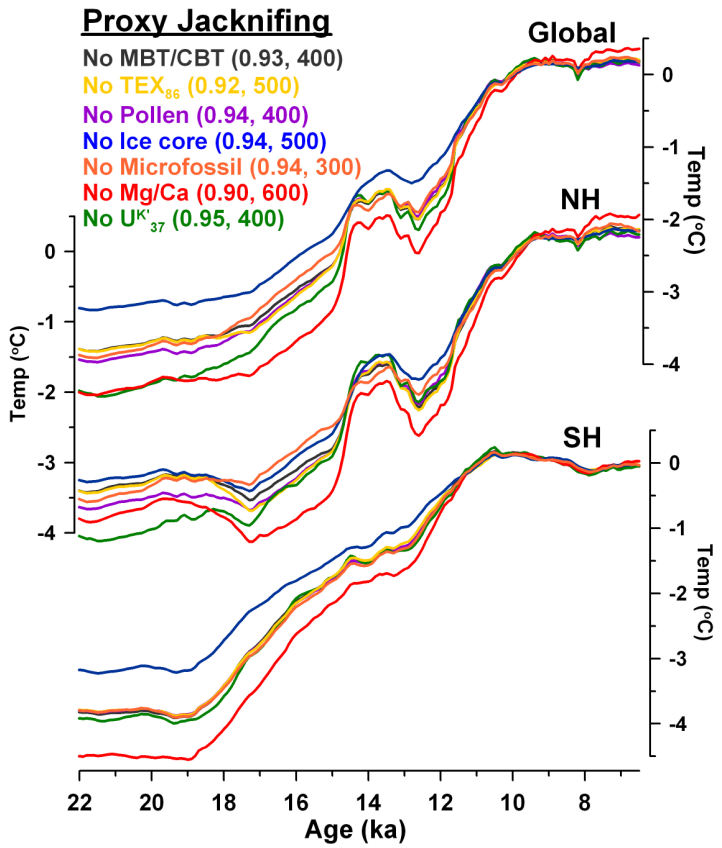

Figure S18: Jackknifing by proxy type. Jackknifed (**top**) global, (**middle**) Northern Hemisphere, and (**bottom**) Southern Hemisphere temperature stacks, leaving one proxy type out at a time. Numbers in parentheses give global stack correlation (r^2) with CO_2 from 22-6.5 ka and lag behind CO_2 (years) determined from lag correlations over 20-10 ka. Note that these stacks are not area-weighted.

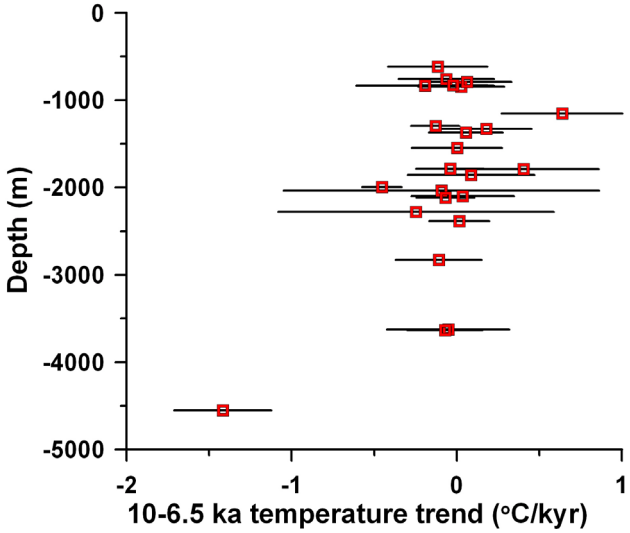

Figure S19: Early Holocene (10-6.5 ka) temperature trends in Mg/Ca records plotted against core depth. Errors (1σ) reflect age-model and temperature calibration uncertainties.

In Figure S20 we plot the 21.5-19 and 19-17.5 ka temperature trends by proxy type to better diagnose the source of the early, pre-CO_2-rise warming. Greenland warming stands out during the earlier interval, with few other records outside of the northern extratropics exhibiting temperature trends significantly different from zero. During the later interval, the interhemispheric seesaw event is evident and seen in multiple proxies. Nonetheless, there are some notable differences among the proxies from 19-17.5 ka. Three TEX_{86} and one MBT/CBT record from 10-35°N warm strongly as compared to Mg/Ca, alkenones, and forams. Also, Mg/Ca records from 30°N-30°S generally show greater warming trends than alkenones, averaging 0.37°C/kyr versus 0.03°C/kyr. Thus, the warming of the northern tropics during this interval, and the resulting net global warming, may be largely attributable to Mg/Ca and TEX_{86}.

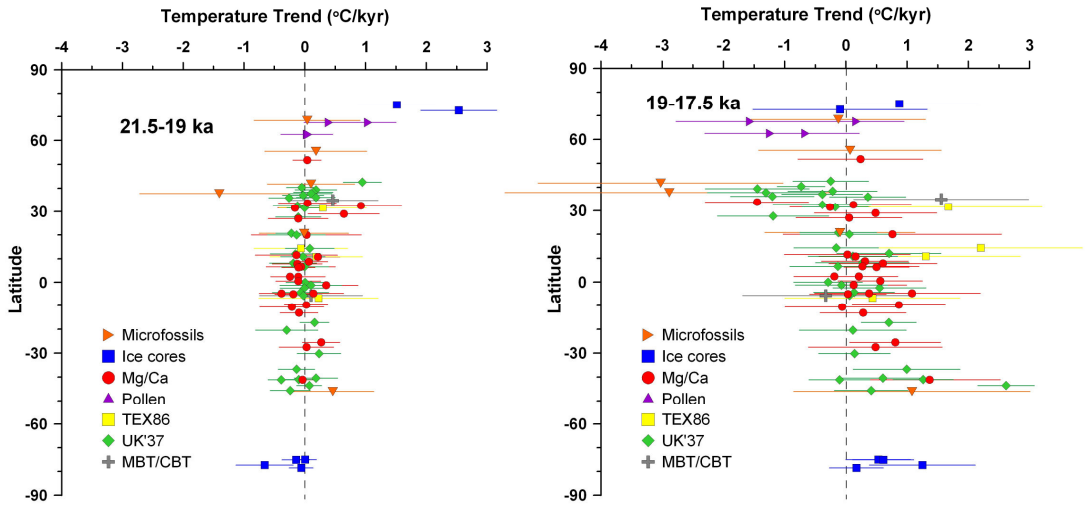

Figure S20: Site-by-site early deglacial temperature trends. Linear temperature trends versus latitude from (**left**) 21.5-19 ka and (**right**) 19-17.5 ka plotted by proxy type. Errors (1σ) reflect age-model and temperature calibration uncertainties.

5.4 Missing data values

There is nearly complete data coverage of the study interval; however, ~15% of the records do not extend entirely through the Last Glacial Maximum and early Holocene

(Figure S1c). To address this issue, we used the Regularized Expectation Maximization (RegEM) method[78] to statistically infill missing values. This adjustment has negligible impact on the temperature stack. We use the infilled data in the main paper.

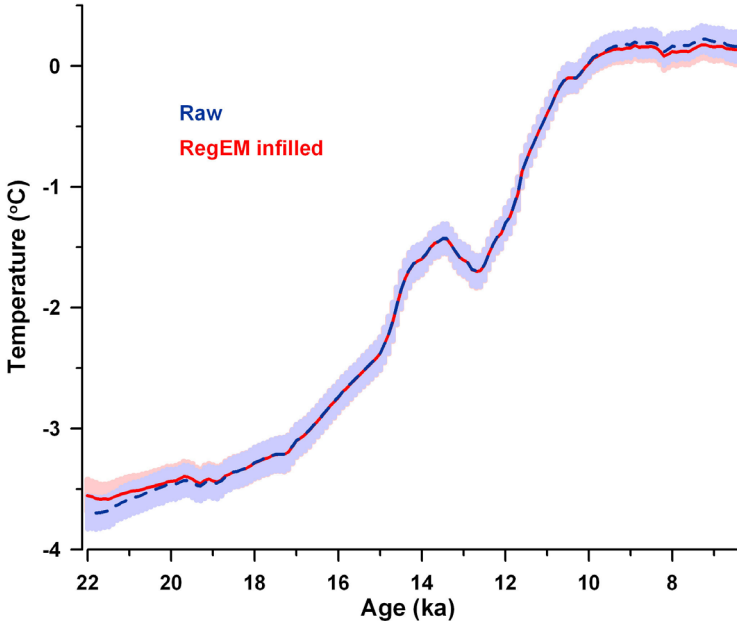

Figure S21: Raw versus infilled temperature data. The temperature stack based on the raw (blue) and statistically-infilled (red) datasets. Errors (1σ) reflect age-model and temperature calibration uncertainties.

5.5 Radiocarbon calibration

67 of the 80 proxy records are anchored solely by radiocarbon dates. We tested the sensitivity of the temperature stack to the choice of radiocarbon calibration by recalibrating all dates with the two most recent calibrations, IntCal04 and IntCal09. While these calibrations are very similar over most of their duration, they differ by up to nearly 1-kyr during the Heinrich-1 interval (Figure S22). Accordingly, the two calibrations yield essentially identical temperature stacks except during Heinrich 1, when they are offset by ~350 years (Figure S23). We reason that the stack is shifted by only 350 years, rather than the full 1-kyr difference between the calibrations, because many of

the proxy records do not have radiocarbon dates in this interval and thus are unaffected. Nonetheless, this offset is important, especially as it occurs during the initial rise in CO_2. For instance, while CO_2 generally leads the temperature stack from 20-10 ka regardless of the calibration, the lead is 460 ± 340 years with IntCal04 but 350 ± 340 years with IntCal09 (Figure S24).

We favor the IntCal04 calibration for the following reasons:

In the IntCal09 paper, Reimer et al.[79] wrote that "the Iberian Margin data generally agree within 2 standard deviations with the Cariaco data and other calibration data. The only notable discrepancy occurs between 15–17.5 cal ka, corresponding to the Heinrich 1 climatic event. This systematic difference could be suppressed by assuming a larger reservoir age for the Iberian Margin. However, such ad hoc corrections may not apply since available data measured on other archives (the few corals in Figure 2 and Bahamas speleothem by Hoffmann et al. [2010]) support the Iberian Margin record. Like the Cariaco record, the present MD952042 [Iberian] chronology must be considered a work in progress awaiting refinement by correlation with more independent data from other archives (corals, speleothems,and marine cores from other oceans)."

Two recent studies have confirmed that the Iberian margin dating is indeed correct. Specifically, climate records developed from deep-sea sediments from the Pakistan Margin can be securely tuned to the Hulu $\delta^{18}O$ record[80] and a new ^{14}C-U/Th dataset generated with coral samples cored offshore Tahiti[81] demonstrate that IntCal04 was more accurate than IntCal09 in the time range corresponding to the early deglaciation, notably the Heinrich 1 event and Oldest Dryas period. The discrepancy can be illustrated by calibrating a ^{14}C age of 13.5 ka BP, which is about 16 cal ka BP with

IntCal04 and 17 cal ka BP with IntCal09 (see Figure S22 that compiles the IntCal09 dataset together with some additional data from the Pakistan Margin).

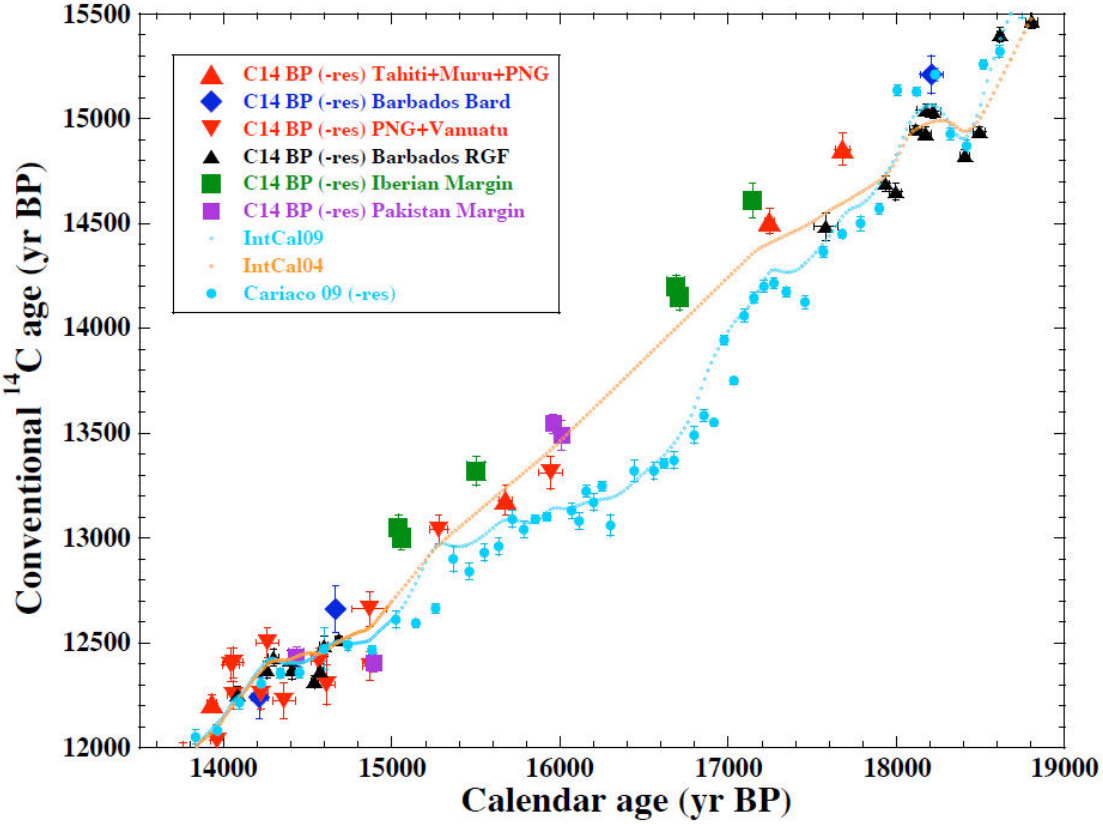

Figure S22: ^{14}C ages plotted versus calendar ages in the interval between 13,500 and 19,000 cal yr BP. Blue diamonds, red and black triangles show the coral data from Barbados, Tahiti, Mururoa, New Guinea and Vanuatu corals. These datasets were used to construct the IntCal09 curve (see Reimer et al.[79] and references therein for the individual records). The light blue dots, green and purple squares show ^{14}C results on planktonic foraminifera from marine sediments tuned to the Hulu speleothem δ^{18}O record independently dated with U-Th ages (the Cariaco Basin and Iberian Margin datasets were also used for constructing the IntCal09 curve, the new Pakistan Margin results are from Bard et al.[80]). All ^{14}C ages are corrected for site-specific reservoir ages (see Reimer et al.[79]) and errors are quoted at the 1σ level. Dotted lines show the resulting calibration curves: in light blue the IntCal09 curve[78] and in orange the previous IntCal04 curve[79] that did not take into account the Cariaco data in this time range (see discussion in Reimer et al.[79]).

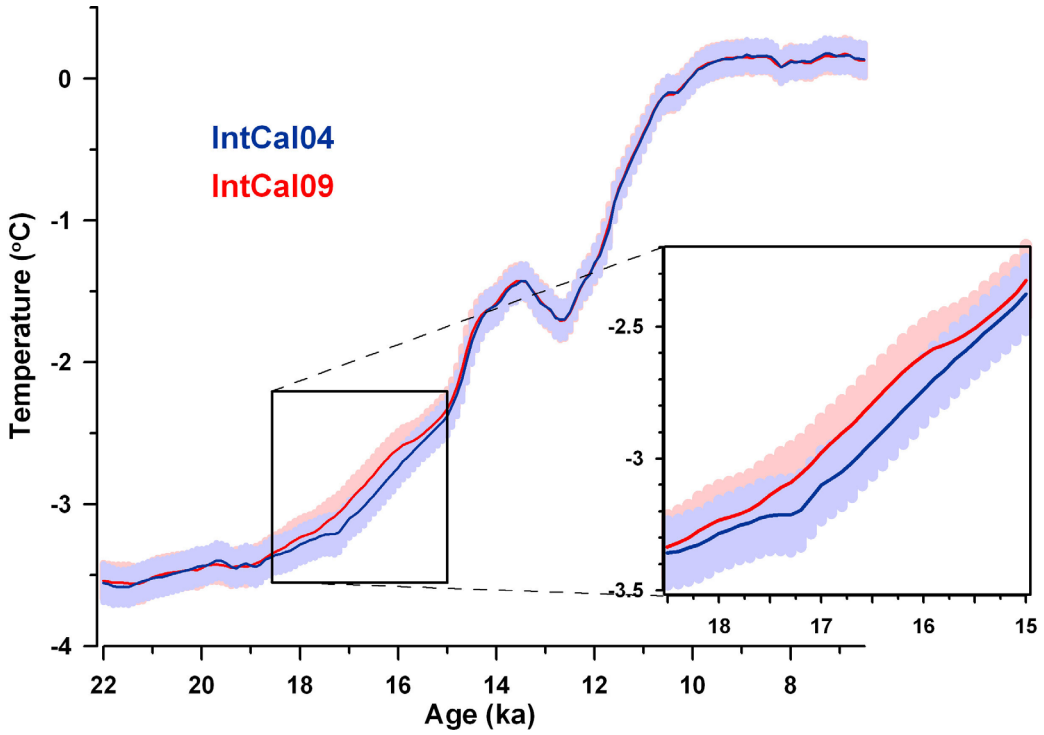

Figure S23: The proxy temperature stack based on the IntCal04 and IntCal09 radiocarbon calibrations. The inset plot shows the interval of disagreement from 18.5-15 ka. Errors (1σ) reflect age-model and temperature calibration uncertainties.

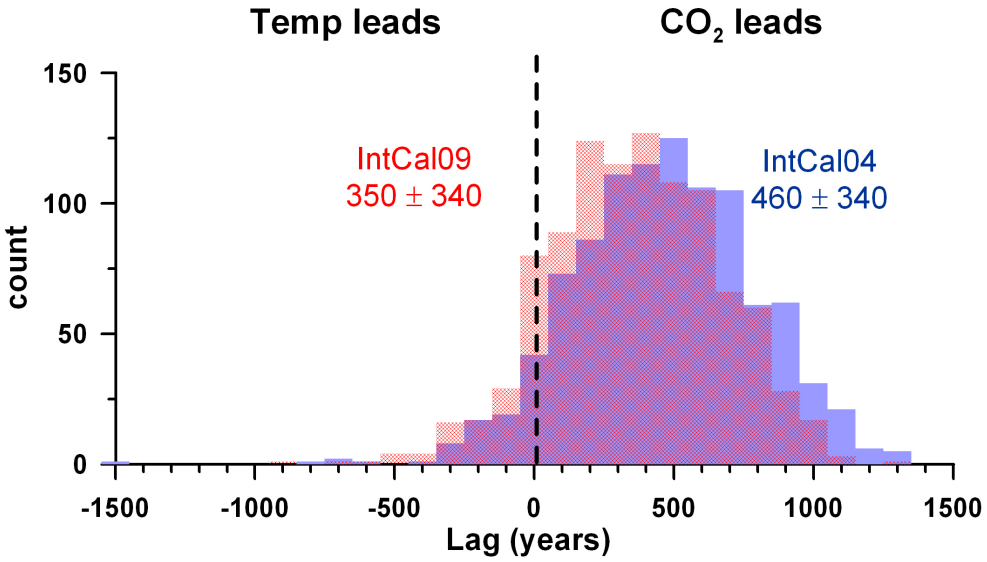

Figure S24: CO_2-temperature phasing based on IntCal04 and IntCal09. The phasing of CO_2 and the global proxy temperature stack based on the IntCal09 (red) and IntCal04 (blue) radiocarbon calibrations using lag correlations from 20-10 ka. The histograms show the result of 1000 realizations, perturbing the proxy records with age model and temperature uncertainties and the CO_2 record with age model errors. The mean and standard deviation of the histograms are given.

6. CO_2-temperature relationship

6.1 Phasing through time

In the main text we discuss the phasing of CO_2 and temperature over the entire 20-10 ka interval. Here, we calculate running phase relationships between CO_2 and the global temperature stack as well as EDC temperature to address how phasing may have varied through time. Phasing is calculated using lag correlations, and we vary time window widths from 3 to 7 kyr. The results indicate Antarctic temperature led CO_2 by a small amount throughout the deglaciation (Figure S25a). The global temperature stack, on the other hand, was synchronous with or lagged CO_2, except at the onset of deglaciation when it led (Figure S25b).

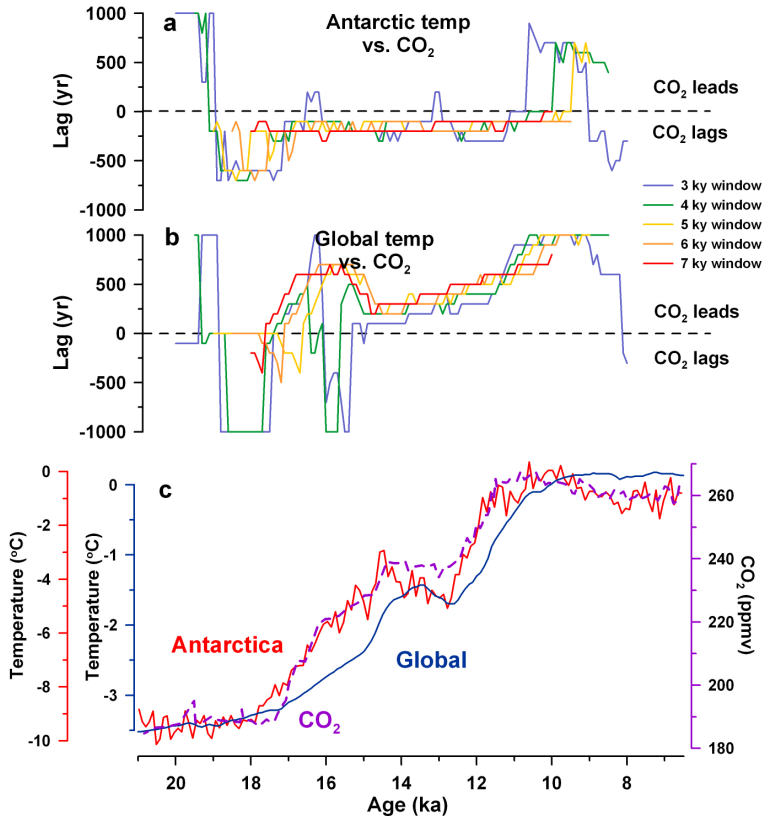

Figure S25: Running temperature-CO_2 lag correlations. (a) Running phasing of CO_2 and EPICA Dome C over the last deglaciation, both on the timescale from ref. 64. The different colors indicate the window width used to compute lag correlations. **(b)** Same as (a), but for CO_2 and the global temperature stack. **(c)** The time series used in (a) and (b).

6.2 Breakfit

While we focus on lag correlations to determine phasing in the main text, here we include an alternative evaluation of this issue. The function Breakfit[82] provides an objective identification of transition points in time series, which allows us to assess the relative timing of changes in the CO_2 and global temperature records. We determine the timing of four transition points in the records and apply the same search windows to both time series for consistency. The same seed generator number (200) is used in each case, 200 bootstrap iterations are used to quantify errors, and standard deviations of 0.15°C and 3 ppmv are used for temperature and CO_2. The results indicate that CO_2 was either synchronous within error or led temperature at the starts of the deglaciation, Bølling, and Younger Dryas, and Holocene (Figure S26; Table S2).

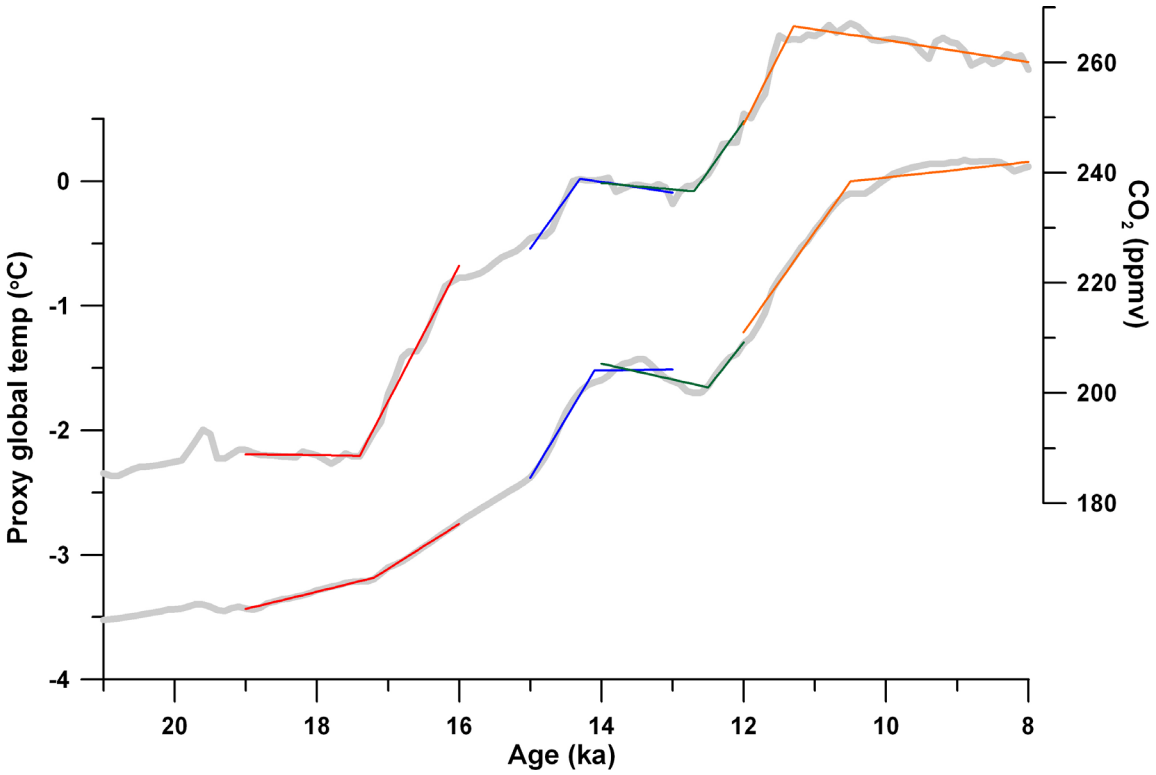

Figure S26: Objectively defined change-points. Breakfit[82] functions (colored lines) applied to the CO_2 (top) and global temperature stack (bottom).

Table S2: Breakfit[82] identification of deglacial transition points. Errors are 1σ.

		CO_2	Temperature
Event	Search window	Age (ka)	Age (ka)
Deglacial onset	19-16 ka	17.40 ± 0.03	17.20 ± 0.03
Bølling	15-13 ka	14.29 ± 0.06	14.10 ± 0.06
Younger Dryas	14-12 ka	12.70 ± 0.06	12.50 ± 0.08
Holocene	12-8 ka	11.29 ± 0.05	10.8 ± 0.04

6.3 Detrending

Tests with synthetic time series suggest that detrending records with ramp structures can increase the resolving power of lag correlations to determine lead-lag relationships (Figure S27). Lag correlations between CO_2 and the global temperature stack from 20-10 ka after detrending yield similar results to those for the undetrended time series presented in Figure 1b in the main paper (Figure S28).

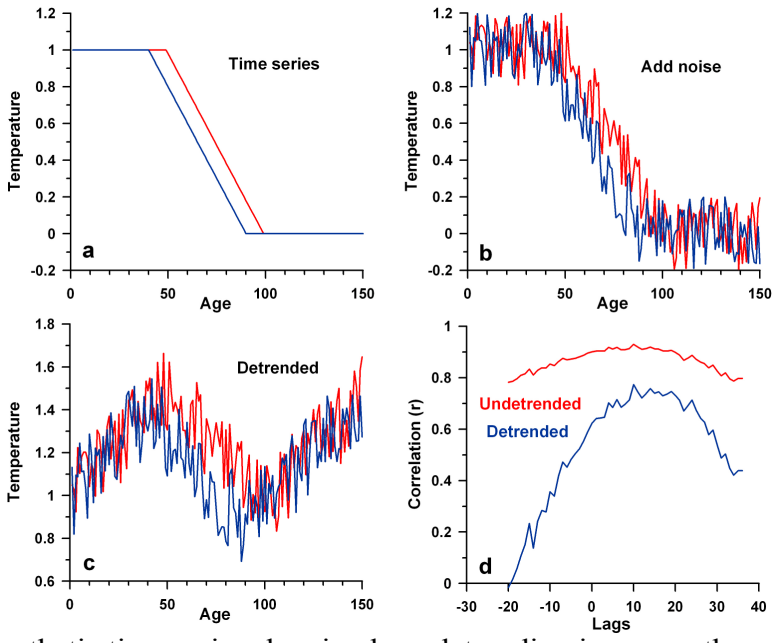

Figure S27: Synthetic time series showing how detrending increases the resolving power of lag correlations. (**a**) Ramped time series with a 10 unit phase offset. (**b**) With noise added. (**c**) Linearly detrended. (**d**) Lag correlations between the detrended (blue) and undetrended (red) noisy time series.

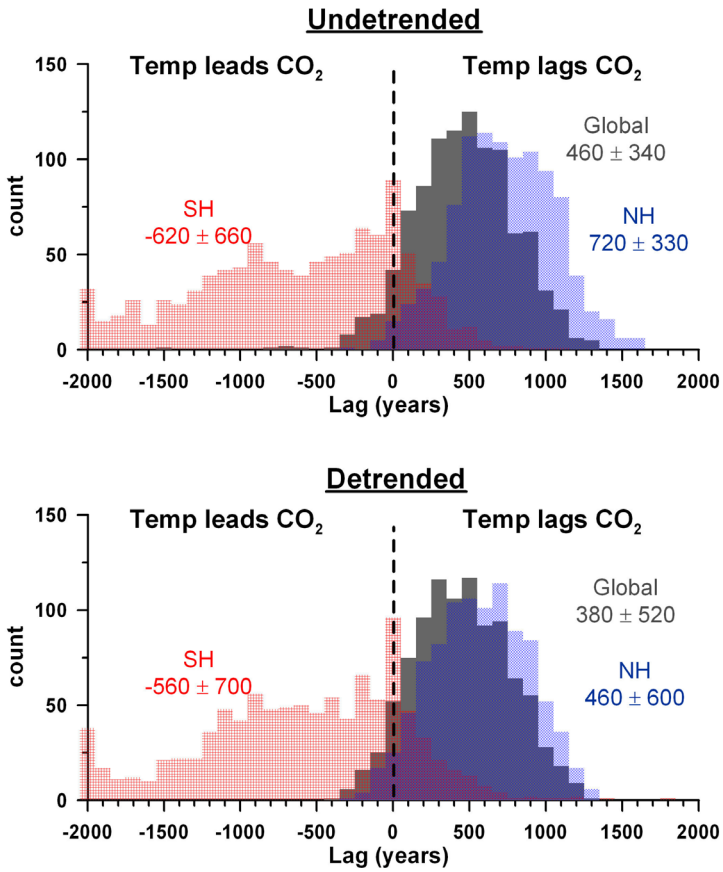

Figure S28: CO_2-temperature phasing using raw and detrended time series. Histograms showing the lead-lag relationship based on lag correlations from 20-10 ka between CO_2 and the proxy global (gray), Northern Hemisphere (blue), and Southern Hemisphere (red) temperature stacks before (top) and after (bottom) detrending. The histograms show the results of 1000 realizations after perturbing the temperature records with age model and proxy temperature errors and the CO_2 record with age model errors. The mean and standard deviation of each histogram are given.

6.4 CO_2 versus CO_2+CH_4+N_20

While we focus on CO_2 in the manuscript since it dominated the deglacial greenhouse gas forcing (Figure S29), CH_4 and N_2O are also globally well-mixed greenhouse gases and would be expected to affect global temperature. The correlations of the global temperature stack with CO_2 forcing and combined CO_2+CH_4+N_2O forcing are similar (r^2=0.94 and 0.93), as are the temperature lags behind each (460±340 yr and

250±340) (Figure S29), supporting our conclusion that greenhouse gases were an important driver of deglacial warming.

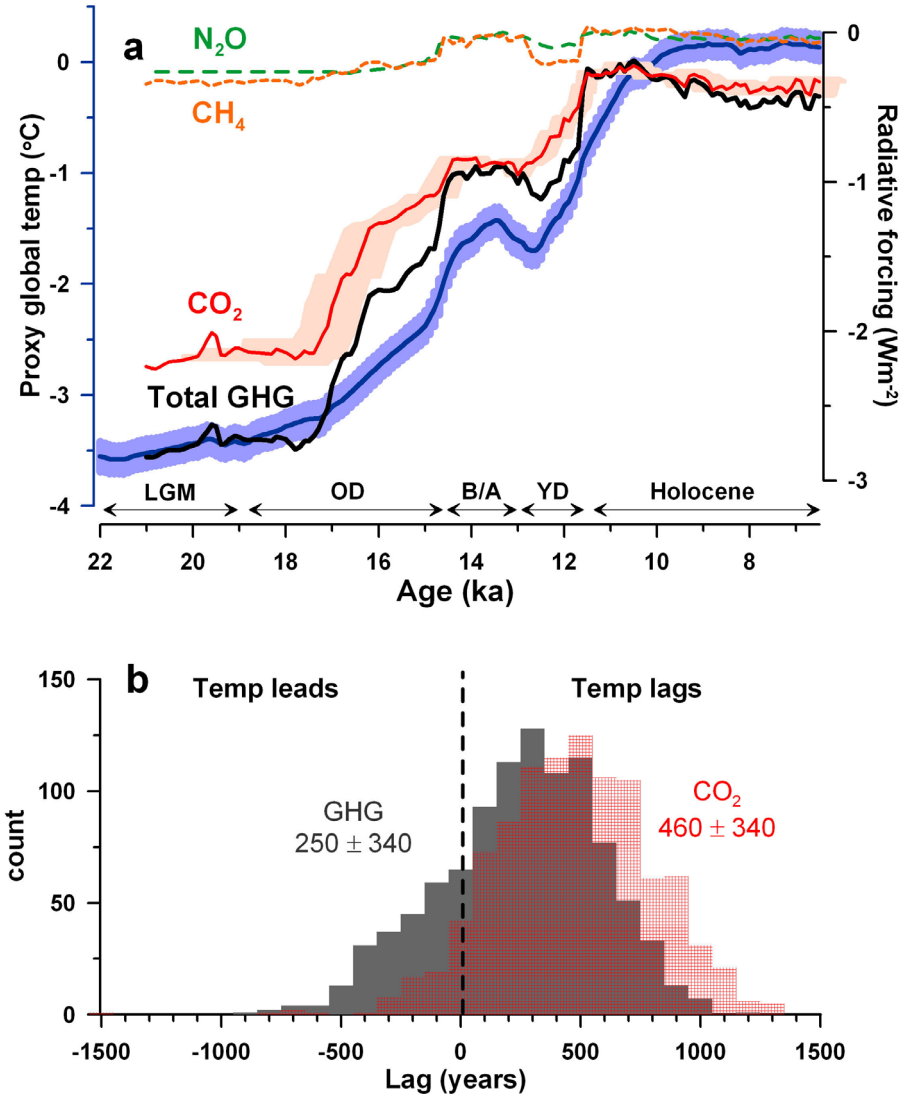

Figure S29: Global temperature stack versus greenhouse-gas forcing. (**a**) The global temperature stack (blue), and the radiative forcing from N_2O (dashed green), CH_4 (dotted orange), and CO_2 (solid red), as well as their combined forcing (thick black) using the simplified expressions from ref. 83. CO_2 age-model uncertainty (1σ) is shown (see section 2.3). (**b**) The phasing of the global temperature stack with CO_2 (red) and combined greenhouse gas-forcing (gray) based on lag correlations from 20-10 ka. 1000 realizations are shown, perturbing the proxy records with age model and temperature errors, and the CO_2 and combined greenhouse gas-forcing curves with CO_2 age model errors (see Section 2.3). The mean and standard deviation of the histograms are given.

7. Model freshwater forcing

As emphasized in the paper, several model freshwater forcing scenarios were tested, and the scenario that produced North Atlantic climate variability in closest agreement with proxy records was used for the final simulation (Figure S30).

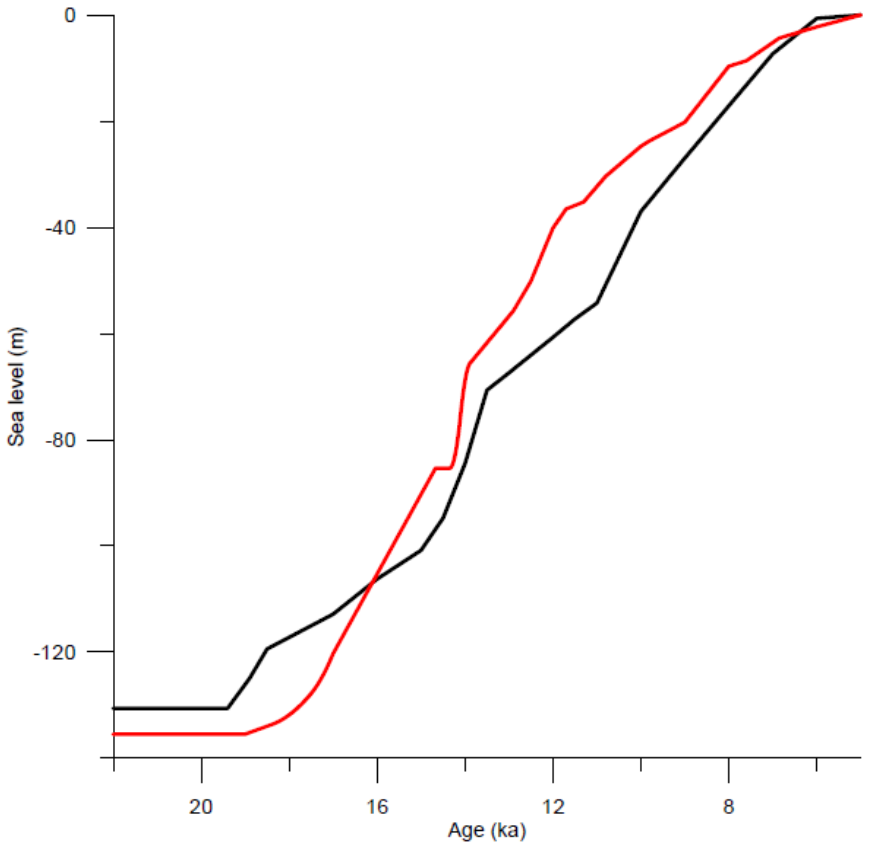

Figure S30: The freshwater flux added to the model shown as equivalent sea level (red) and reconstructed eustatic sea level[84] (black).

8. Comparison with Schmittner et al. (2011)[85]

The glacial-interglacial warming in our proxy temperature stack is ~3.6°C, which is larger than a recent estimate of 2.6°C by Schmittner et al.[85]. We examine here the reasons for this difference. Fundamentally, the data used in this study are a small subset of the much larger LGM dataset used by Schmittner et al., which also included the MARGO[86] sea-surface and Bartlein et al.[87] continental temperature reconstructions (80 individual reconstructions in this study versus 1,100 in Schmittner et al.). As the Schmittner et al. results are strongly influenced by MARGO, we compared the consistency of our dataset with MARGO at the 35 5° x 5° grid cells where both have data, which range from 57.5°N to 47.5°S. Of these 35 grid cells, 22 have completely independent data (i.e., our proxy records at these locations are not included in MARGO) while 13 have redundant data (i.e., our proxy records at these locations are included in MARGO, in addition to others). The area-weighted mean LGM cooling at the 22 cells containing entirely independent data is -3.1°C for MARGO and -2.9°C for our dataset (n=9 Mg/Ca, n=15 alkenones, n=3 foram assemblages n=3 TEX_{86}), and -3.2°C for both MARGO and our dataset (n=4 Mg/Ca, n=8 alkenones, n=1 foram assemblage) at the 13 cells containing redundant data (Table S3). Since MARGO has a global SST cooling of -1.9±1.8°C, the larger cooling at our grid cells suggests that our ocean data are biased toward more sensitive sites. In summary, where we have common ocean data coverage, our results are in close agreement with the Schmittner et al. dataset (i.e., MARGO), but the greater spatial data coverage in Schmittner et al. versus this study and Shakun and Carlson[88] indicates that the Schmittner et al. data are more representative of the LGM to modern temperature difference.

Table S3: Last Glacial Maximum temperature anomalies

	Model	**Proxy data**		
	Schmittner et al.[85]	This study	MARGO[86]	Bartlein et al.[87]
SST ocean	-1.7±0.4°C *	-3.2°C (n=53) ^	-1.9±1.8°C (n=307)	-
SAT land	-4.6±0.7°C **	-6.4°C (n=14) ^	-	-6.1°C (n=98)
SST shared ocean grid cells (independent data)	-	-2.9°C (n=22) ^^	-3.1°C (n=22)	-
SST shared ocean grid cells (redundant data)	-	-3.2°C (n=13) ^^	-3.2°C (n=13)	-
SAT global land+ SST global ocean	-2.6±0.5°C ***	-	-	-
SAT global land+ SAT global ocean	-3.3±0.5°C ****	-	-	-

"SAT" = surface air temperature. "SST" = sea surface temperature. "n" is number of grid cells; Schmittner et al., this study, and MARGO are based on a 5° x 5° grid, while Bartlein et al. is on a 2° x 2° grid.

* global model mean (interpolated to median of PDF) 66% interval = [-1.3;-2.0]

** global model mean (interpolated to median of PDF) 66% interval = [-3.9:-5.2]

*** global model mean (interpolated to median of PDF) 66% interval = [-2.0:-2.9]

**** global model mean (interpolated to median of PDF) 66% interval = [-2.4:-3.5]

^ LGM (19-23 ka) anomalies from early Holocene (6.5-10.5 ka) mean

^^ LGM (19-23 ka) anomalies from late Holocene (2-0 ka) mean for proxy records that extend to present or WOA98 (ref. 89) 10-m depth temperatures for records that end before 2 ka.

References

1. Cuffey, K. M. & Clow, G.D. Temperature, accumulation, and ice sheet elevation in central Greenland through the last deglacial transition. *J. of Geophy. Res.* **102**, 26383-26396 (1997).
2. Andersen, K. K. *et al.* The Greenland Ice Core Chronology 2005, 15-42 ka. Part 1: Constructing the time scale. *Quat. Sci. Rev.* **25**, 3246-3257, doi:10.1016/j.quascirev.2006.08.002 (2006).
3. Rasmussen, S. O. *et al.* A new Greenland ice core chronology for the last glacial termination. *J. Geophys. Res.* **111**, doi:10.1029/2005JD006079 (2006).
4. Rasmussen, S. O. *et al.* Synchronization of the NGRIP, GRIP, and GISP2 ice cores across MIS 2 and palaeoclimatic implications. *Quat. Sci. Rev.* **27**, 18-28, doi:10.1016/j.quascirev.2007.01.016 (2008).
5. Kurek, J., Cwynar, L. C., Ager, T. A., Abbott, M. B. & Edwards, M. E. Late Quaternary paleoclimate of western Alaska inferred from fossil chironomids and its relation to vegetation histories. *Quat. Sci. Rev.* **28**, 799-811 (2009).
6. Viau, A.E., Gajewski, K., Sawada, M. C. & Bunbury, J. Low-and high frequency climate variability in Eastern Beringia during the past 25,000 years. *Canadian J. Earth Sci.* **45**, 1435-1453 (2008).
7. Waelbroeck, C. *et al.* The timing of the last deglaciation in North Atlantic climate records. *Nature* **412**, 724-727 (2001).
8. Peck, V. L., Hall, I. R., Zahn, R. & Elderfield, H. Millennial-scale surface and subsurface paleothermometry from the northeast Atlantic, 55-8 ka BP. *Paleoceanography* **23**, doi:10.1029/2008PA001631 (2008).
9. Prahl, F.G., Pisias, N. G., Sparrow, M. A. & Sabin, A. Assessment of sea-surface temperature at 42 degrees north in the California current over the last 30,000 years. *Paleoceanography* **10**, 763-773 (1995).
10. Minoshima, K, Kawahata, H. & Ikehara, K. Changes in biological production in the mixed water region of the northwestern North Pacific during the last 27 kyr. *Palaeogeog. Palaeoclim. Palaleoecol.* **254**, 430-447 (2007).
11. Cacho, I., Grimalt, J. O., Canals, M., Sbaffi, L. & Shackelton, N. J. Variability of the western Mediterranean Sea surface temperature during the last 25,000 years and its connection with the Northern Hemisphere climatic changes. *Paleoceanography* **16,** 40-52 (2001).
12. Bard, E., Rostek, F., Turon, J.-L. & Gendreau, S. Hydrological impact of Heinrich events in the subtropical northeast Atlantic. *Science* **289,** 1321-1324 (2000).
13. Calvo, E. Villanueva, J., Grimalt, J. O., Boelaert, A. & Labeyrie, L. New insights into the glacial latitudinal temperature gradients in the North Atlantic. Results from $U^{K'}_{37}$ sea surface temperatures and terrigenous inputs. *Earth Planet Sci. Lett.* **188**, 509–519 (2001).
14. Cacho, I. *et al.* Dansgaard-Oeschger and Heinrich Event imprints in Alboran Sea paleotemperatures. *Paleoceanography* **14,** 698-705 (1999).
15. Isono, D. *et al.* The 1500-year climate oscillation in the midlatitude North Pacific during the Holocene. *Geology* **37**, 591-594 (2009).
16. Peterse, F. *et al.* Decoupled warming and monsoon precipitation in East Asia over the last deglaciation. *Earth Plan. Sci. Lett.* **301**, 256-264 (2011).

17. Carlson, A. E. *et al.* Subtropical salinity variability and Atlantic meridional circulation during deglaciation. *Geology* **12**, 991-994 (2008).
18. Sawada, K. & Handa, N. Variability of the path of the Kuroshio ocean current over the past 25,000 years. *Nature* **392**, 592-595 (1998).
19. Castañeda, I.S. *et al.* Millennial-scale surface temperature changes in the eastern Mediterranean (Nile River Delta region) over the last 27,000 years. *Paleoceanography* **25**, PA1208, doi:10.1029/2009PA001740 (2010).
20. Kubota, Y. *et al.* Variations of East Asian summer monsoon since the last deglaciation based on Mg/Ca and oxygen isotope of planktonic foraminifera in the northern East China Sea. *Paleoceanography* **25**, PA4205, doi:10.1029/2009PA001891 (2010).
21. Ijiri, A. *et al.* Paleoenvironmental changes in the northern area of the East China Sea during the past 42,000 years. *Palaeogeog. Palaeoclim. Palaleoecol.* **219**, 239-261 (2005).
22. Ziegler, M., Nürnberg, D., Karas, C., Tiedemann, R. & Lourens, L. J. Persistent summer expansion of the Atlantic Warm Pool during glacial abrupt cold events. *Nature Geo.* **1**, 601-605 (2008).
23. Arz, H. W., Pätzold, J., Müller, P. J. & Moammar, M. O. Influence of Northern Hemisphere climate and global sea level rise on the restricted Red Sea marine environment during termination I, *Paleoceanography* **18**, 1053, doi:10.1029/2002PA000864 (2003).
24. Flower, B. P., Hastings, D. W., Hill, H. W. & Quinn, T. M. Phasing of deglacial warming and Laurentide Ice Sheet meltwater in the Gulf of Mexico. *Geology* **32,** 597-600 (2004).
25. deMenocal, P. B., Ortiz, J., Guilderson, T. & Sarnthein, M. Coherent high- and low-latitude climate variability during the Holocene warm period. *Science* **288,** 2198-2202 (2000).
26. Zhao, M., Beveridge, N., Shackleton, N., Sarnthein, M. & Eglington, G. Molecular stratigraphy of cores off northwest Africa: Sea surface temperature history over the last 80ka. *Paleoceanography* **10,** 661-675 (1995).
27. Pelejero, C., Grimalt, J. O., Heilig, S., Kienast, M. & Wang, L. High-resolution U^{k}_{37} temperature reconstructions in the South China Sea over th past 220 kyr. *Paleoceanography* **14,** 224-231 (1999).
28. Wei, G., Deng, W., Liu, Y. & Li, X. High-resolution sea surface temperature records derived from foraminiferal Mg/Ca ratios during the last 260 ka in the northern South China Sea. *Palaeogeog. Palaeoclim. Palaleoecol.* **250**, 126-138 (2007).
29. Huguet, C., J.-H. Kim, J. S. S. Damste´ & S. Schouten. Reconstruction of sea surface temperature variations in the Arabian Sea over the last 23 kyr using organic proxies (TEX_{86} and $U^{K'}_{37}$). *Paleoceanography* **21**, PA3003, doi:10.1029/2005PA001215 (2006).
30. Rühlemann, C., Mulitza, S., Muller, P. J., Wefer, G. & Zahn, R. Warming of the tropical Atlantic Ocean and slowdown of thermohaline circulation during the last deglaciation. *Nature* **402,** 511-514 (1999).

31. Schmidt, M. W., Spero, H. J. & Lea, D. W. Links between salinity variation in the Caribbean and North Atlantic thermohaline circulation. *Nature* **428,** 160-163 (2004).
32. Lea, D. W., Pak, D. K., Peterson, L. C. & Hughen, K. A. Synchroneity of tropical and high-latitude Atlantic temperatures over the last glacial termination. *Science* **301,** 1361-1364 (2003).
33. Rosenthal, Y., Oppo, D. & Linsley, B. K. The amplitude and phasing of climate change during the last deglaciation in the Sulu Sea, western equatorial Pacific. *Geophys. Res. Lett.* **30,** doi:10.1029/2002GL016612 (2003).
34. Leduc, G. *et al.* Moisture transport across Central America as a positive feedback on abrupt climatic changes. *Nature* **445**, 908-911 (2007).
35. Benway, H. M., Mix, A. C., Haley, B. A. & Klinkhammer, G. P. Eastern Pacific warm pool paleosalinity and climate variability: 0-30 kyr. *Paleoceanography* **21,** doi:10.1029/2005PA001208 (2006).
36. Steinke, S. *et al.* Proxy dependence of the temporal pattern of deglacial warming in the tropical South China Sea: toward resolving seasonality. *Quat. Sci. Rev.* **27**, 688-700 (2008).
37. Stott, L., Timmermann, A. & Thunell, R. Southern hemisphere and deep-sea warming led deglacial atmospheric CO_2 rise and tropical warming. *Science* **318,** 435-438 (2007).
38. Weldeab, S., Lea, D. W., Schneider, R. R. & Andersen, N. 155,000 years of West African Monsoon and ocean thermal evolution. *Science* **316,** 1303-1307 (2007).
39. Weldeab, S., Schneider, R. R., Kölling, M. & Wefer, G. Holocene African droughts relate to eastern equatorial Atlantic cooling. *Geology* **33,** 981-984 (2005).
40. Lea, D. W. *et al.* Paleoclimate history of Galápagos surface waters over the last 135,000 yr. *Quat. Sci. Rev.* **25,** 1152-1167 (2006).
41. Kienast, M. *et al.* Eastern Pacific cooling and Atlantic overturning circulation during the last deglaciation. *Nature* **443,** 846-849 (2006).
42. Koutavas, A. & Sachs, J. P. Northern timing of deglaciation in the eastern equatorial Pacific from alkenone paleothermometry. *Paleoceanography* **23**, PA4205, doi:10.1029/2008PA001593 (2008).
43. Koutavas, A., Lynch-Stieglitz, J., Marchitto, T. M., Jr. & Sachs, J. M. El Niño-like pattern in Ice Age tropical Pacific sea surface temperature. *Science* **297,** 226-230 (2002).
44. Jaeschke, A., Rühlemann, C., Arz, H. W., Heil, G. & Lohmann, G. Coupling of millennial-scale changes in sea surface temperature and precipitation off northeastern Brazil with high-latitude climate shifts during the last glacial period. *Paleoceanography* **22**, PA4206, doi:10.1029/2006PA001391 (2007).
45. Weldeab, S., Schneider, R. R. & Kölling, M. Deglacial sea surface temperature and salinity increase in the western tropical Atlantic in synchrony with high latitude climate instabilities. *Earth Planet Sci. Lett.* **241,** 699-706 (2006).
46. Visser, K., Thunell, R. & Stott, L. Magnitude and timing of temperature change in the Indo-Pacific warm pool during deglaciation. *Nature* **421,** 152-155 (2003).

47. Weijers, J. W. H., Schefuß, E., Schouten, S. & Damste, J. S. S. Coupled thermal and hydrological evolution of tropical Africa over the last deglaciation. *Science* **315,** 1701-1704 (2007).
48. Schefuß, E., Schouten, S. & Schneider, R. R. Climatic controls on central African hydrology during the past 20,000 years. *Nature* **437,** 1003-1006 (2005).
49. Tierney, J. E. *et al.* Northern Hemisphere controls on tropical southeast African climate during the past 60,000 years. *Science* **322,** 252-255 (2008).
50. Levi, C. *et al.* Low-latitude hydrological cycle and rapid climate changes during the last deglaciation. *Geochem. Geophys. Geosys.* **8,** doi:10.1029/2006GC001514 (2007).
51. Xu, J., Holbourn, A., Kuhnt, W., Jian, Z. & Kawamura, H. Changes in the thermocline structure of the Indonesian outflow during Terminations 1 and 2. *Earth Planet Sci. Lett.* **273**, 152-162 (2008).
52. Kim, J.-H., Schneider, R. R., Muller, P. J. & Wefer, G. Interhemispheric comparison of deglacial sea-surface temperature patterns in Atlantic eastern boundary currents. *Earth Planet Sci. Lett.* **194,** 383-393 (2002).
53. Bard, E., Rostek, F. & Sonzogni, C. Interhemispheric synchrony of the last deglaciation inferred from alkenone palaeothermometry. *Nature* **385,** 707-710 (1997).
54. Farmer, E. C., DeMendocal, P. B. & Marchitto, T. M. Holocene and deglacial ocean temperature variability in the Benguela upwelling region: Implications for low-latitude atmospheric circulation. *Paleoceanography* **20,** doi:10.1029/2004PA001049 (2005).
55. Kaiser, J., Lamy, F. & Hebbeln, D. A 70-kyr sea surface temperature record off southern Chile (Ocean Drilling Program Site 1233). *Paleoceanography* **20,** doi:10.1029/2005PA001146 (2005).
56. Calvo, E., Pelejero, C., DeDeckker, P. & Logan, G. A. Antarctic deglacial pattern in a 30 kyr record of sea surface temperature offshore South Australia. *Geophys. Res. Lett.* **34**, L13707, doi:10.1029/2007GL029937 (2007).
57. Pahnke, K. & Sachs, J. M. Sea surface temperatures of southern midlatitudes 0–160 kyr B.P. *Paleoceanography* **21,** doi:10.1029/2005PA001191 (2006).
58. Lamy, F. *et al.* Modulation of the bipolar seesaw in the Southeast Pacific during Termination 1. *Earth Planet Sci. Lett.* **259,** 400-413 (2007).
59. Sachs, J. P., Anderson, R. F. & Lehman, S. J. Glacial surface temperatures of the southeast Atlantic Ocean. *Science* **293,** 2077-2079 (2001).
60. Barker, S. *et al.* Interhemispheric Atlantic seesaw response during the last deglaciation. *Nature* **457**, 1097-1102 (2009).
61. Barrows, T. T., Lehman, S. J., Fifield, L. K. & De Deckker, P. Absence of cooling in New Zealand and the adjacent Ocean during the Younger Dryas chronozone. *Science* **318,** 86-89 (2007).
62. Labeyrie, L. *et al.* Hydrographic changes of the Southern Ocean (southeast Indian sector) over the last 230 kyr. *Paleoceanography* **11**, 57-76 (1996).
63. Stenni, B. *et al.* The deuterium excess records of EPICA Dome C and Dronning Maud Land ice cores (East Antarctica). *Quat. Sci. Rev.* **29**, 146-159 (2010).
64. Lemieux-Dudon, B. *et al.* Consistent dating for Antarctic and Greenland ice cores. *Quat. Sci. Rev.* **29**, 8-20 (2010).

65. Kawamura, K. *et al.* Northern Hemisphere forcing of climatic cycles in Antarctica over the past 360,000 years. *Nature* **448,** 912-916 (2007).
66. Petit, J. R *et al.* Climate and atmospheric history of the past 420,000 years from the Vostok ice core, Antarctic. *Nature* **399,** 429-436 (1999).
67. Clark, P. U. *et al.* Global climate evolution during the last deglaciation. *Proc. Natl. Acad. Sci.*, doi:10.1073/pnas.1116619109.
68. Huybers, P & Wunsch, C. A depth-derived Pleistocene age model: Uncertainty estimates, sedimentation variability, and nonlinear climate change. *Paleoceanography* **19**, doi:10.1029/2002PA000857 (2004).
69. Svensson, A. *et al.* A 60 000 year Greenland stratigraphic ice core chronology. *Climate of the Past* **4**, 47-57 (2008).
70. Andersen, K. K. *et al.* The Greenland Ice Core Chronology 2005, 15-42 ka. Part 1: constructing the time scale. *Quat. Sci. Rev.* **25**, 3246-3257 (2006).
71. Pedro, J. B. *et al.* The last deglaciation: timing the bipolar seesaw. *Climate of the Past Discussion* **7**, 397-430 (2011).
72. Blunier, T. *et al.* Synchronization of ice core records via atmospheric gases. *Clim. Past* **3**, 325-330 (2007).
73. Severinghaus, J. P. & Brook, E. J. Abrupt climate change at the end of the last glacial period inferred from trapped air in polar ice. *Science* **286**, 930-934 (1999).
74. Marcott, S. A., Shakun, J. D., Clark, P. U., & Mix, A. C. A reconstruction of Holocene global temperature. *In prep.*
75. Smith, T. M. *et al.* Improvements to NOAA's historical merged land-ocean surface temperature analysis (1880-2006). *J. Clim.* **21**, 2283-2293 (2008).
76. Rayner, N. A. *et al.* Global analyses of sea surface temperature, sea ice, and night marine air temperature since the late nineteenth century. *J. Geophys. Res.* **108**, 4407, doi:10.1029/2002JD002670 (2003).
77. Berger, W. H. Deep-sea carbonate and the deglaciation spike in pteropods and foraminifera. *Nature* **269**, 301-304 (1977).
78. Schneider, T. Analysis of incomplete climate data: Estimation of mean values and covariance matrices and imputation of missing values. *J. Clim.* **14**, 853-871 (2001).
79. Reimer, P. J. *et al.* IntCal09 and Marine09 radiocarbon age calibration curves, 0-50,000 years cal BP. *Radiocarbon* **51**, 1111-1150 (2009).
80. Bard, E., Ménot G. & Licari L. Radiocarbon calibration-comparison records based on marine sediments from the Pakistan and Iberian Margins. *Geophys. Res. Abst.* **11**, EGU2009-6985 (2009).
81. Durand, N *et al.* New insights into the radiocarbon calibration based on 14C and U-Th dating of corals drilled offshore Tahiti (IODP Expedition #310). *Geophys. Res. Abst.* **12**, EGU2010-12689-1 (2010).
82. Mudelsee, M. Break function regression: A tool for quantifying trend changes in climate time series. *Euro. Phys. J. Spec. Top.* **174**, 49-63 (2009).
83. Ramaswamy, V. et al. Radiative forcing of climate change. Climate Change 2001: The Scientific Basis. Contribution of Working Group I to the Third Assessment Report of the Intergovernmental Panel on Climate Change (eds. Houghton, J. T. et al.) (Cambridge Univ. Press, Cambridge, UK, 2001).
84. Clark, P. U. *et al.* The Last Glacial Maximum. *Science* **325**, 710-714 (2009).

85. Schmittner, A. *et al.* Climate sensitivity estimated from temperature reconstructions of the Last Glacial Maximum. *Science* **334**, 1385-1388, doi:10.1126/science.1203513 (2011).
86. MARGO Project Members. Constraints on the magnitude and patterns of ocean cooling at the Last Glacial Maximum. *Nature Geosci.* **2**, 127-132 (2009).
87. Bartlein, P. J. *et al.* Pollen-based continental climate reconstructions at 6 and 21 ka: a global synthesis. *Clim. Dyn.* **37**, doi:10.1007/s00382-010-0904-1.
88. Shakun, J. D. & Carlson, A. E. A global perspective on Last Glacial Maximum to Holocene climate change. *Quat. Sci. Rev.* **29**, 1801-1816 (2010).
89. World Ocean Atlas 1998: <http://ingrid.ldeo.columbia.edu/SOURCES/.NOAA/.NODC/.WOA98/> (NODC, Silver Springs, 1998).

Appendix S1: Age models (blue) with 2σ uncertainties (red lines) for all records based on radiocarbon dating, using the IntCal04 calibration. Radiocarbon dates are shown as black dots.

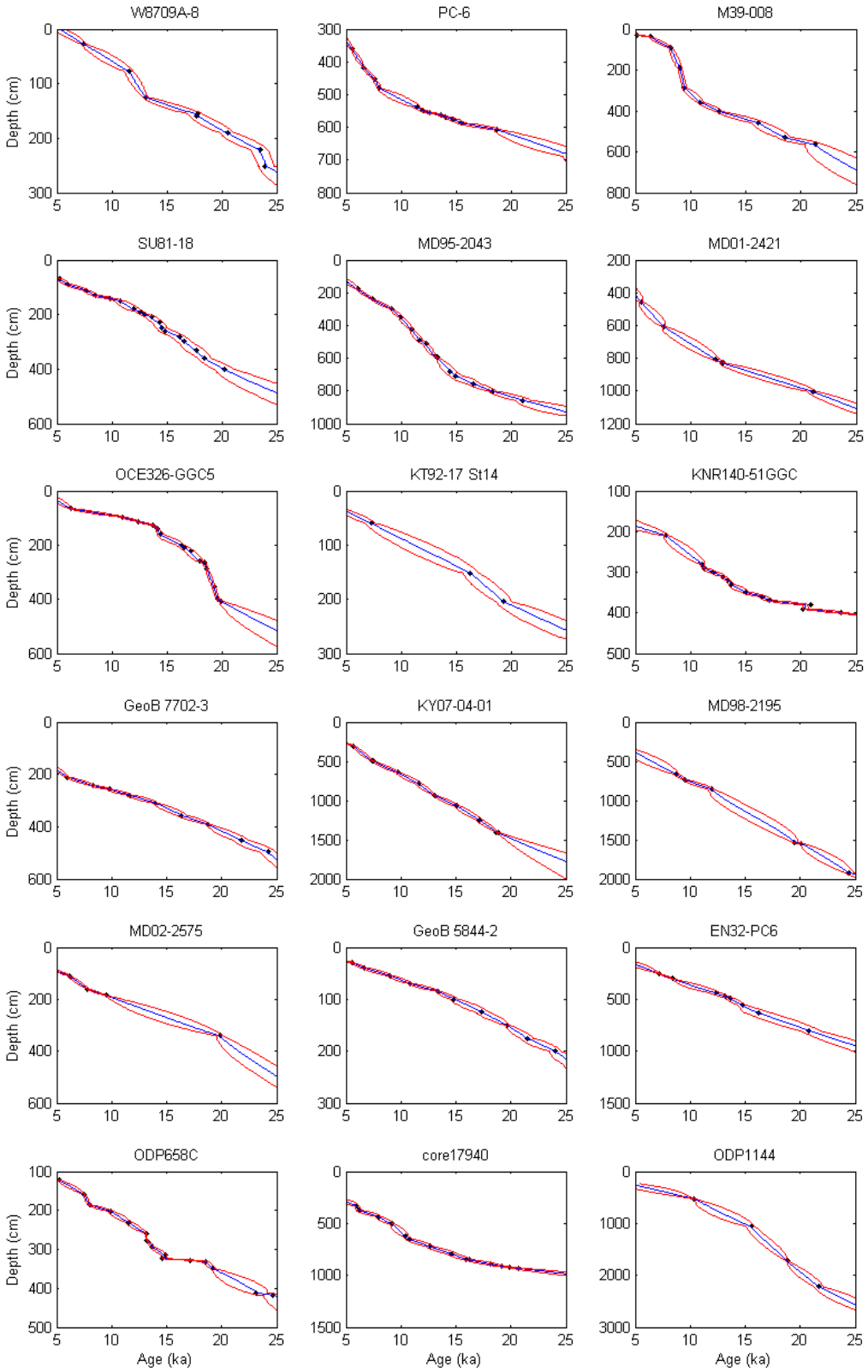

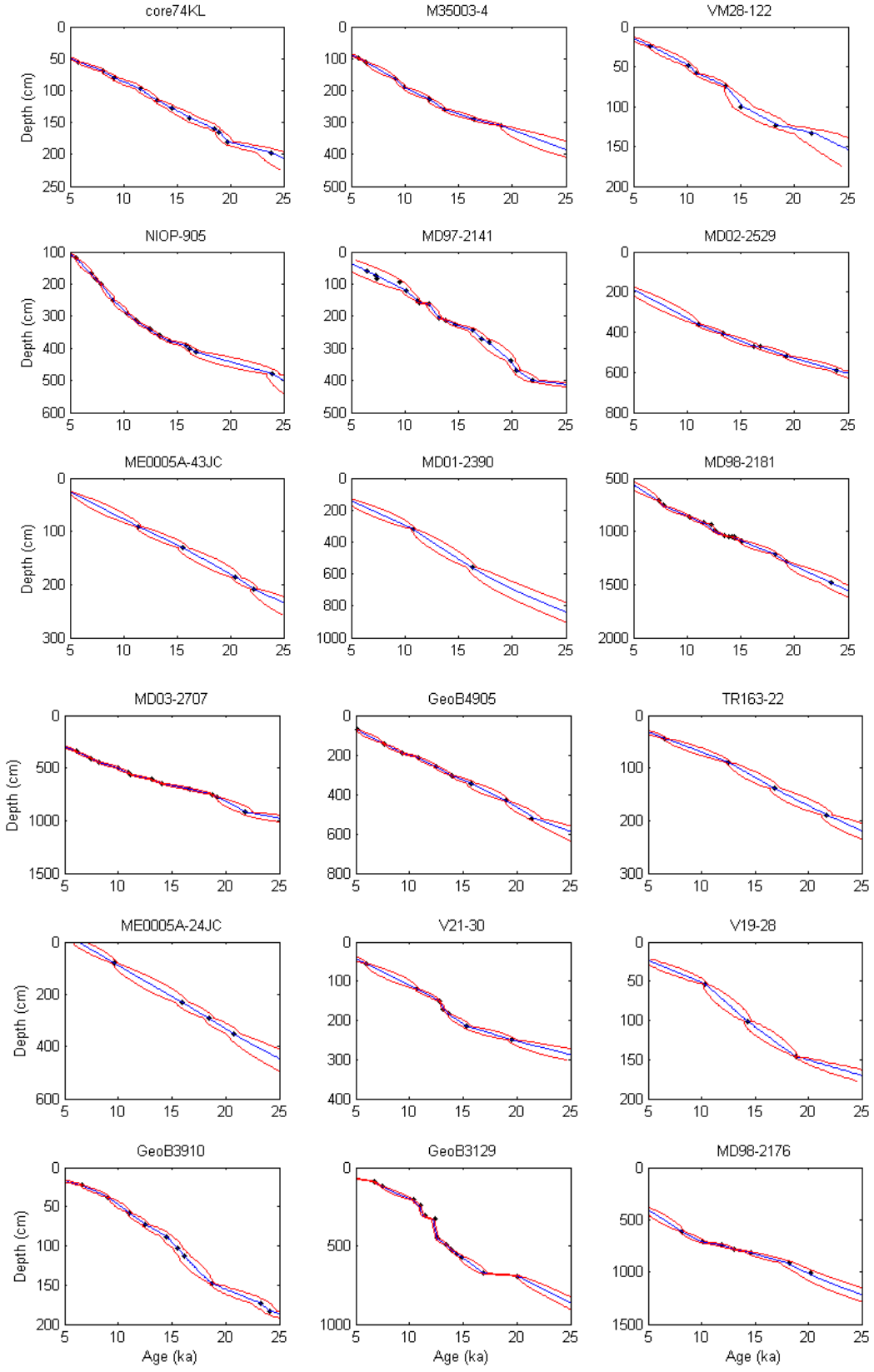
core74KL
M35003-4
VM28-122
NIOP-905
MD97-2141
MD02-2529
ME0005A-43JC
MD01-2390
MD98-2181
MD03-2707
GeoB4905
TR163-22
ME0005A-24JC
V21-30
V19-28
GeoB3910
GeoB3129
MD98-2176
Depth (cm)
Age (ka)

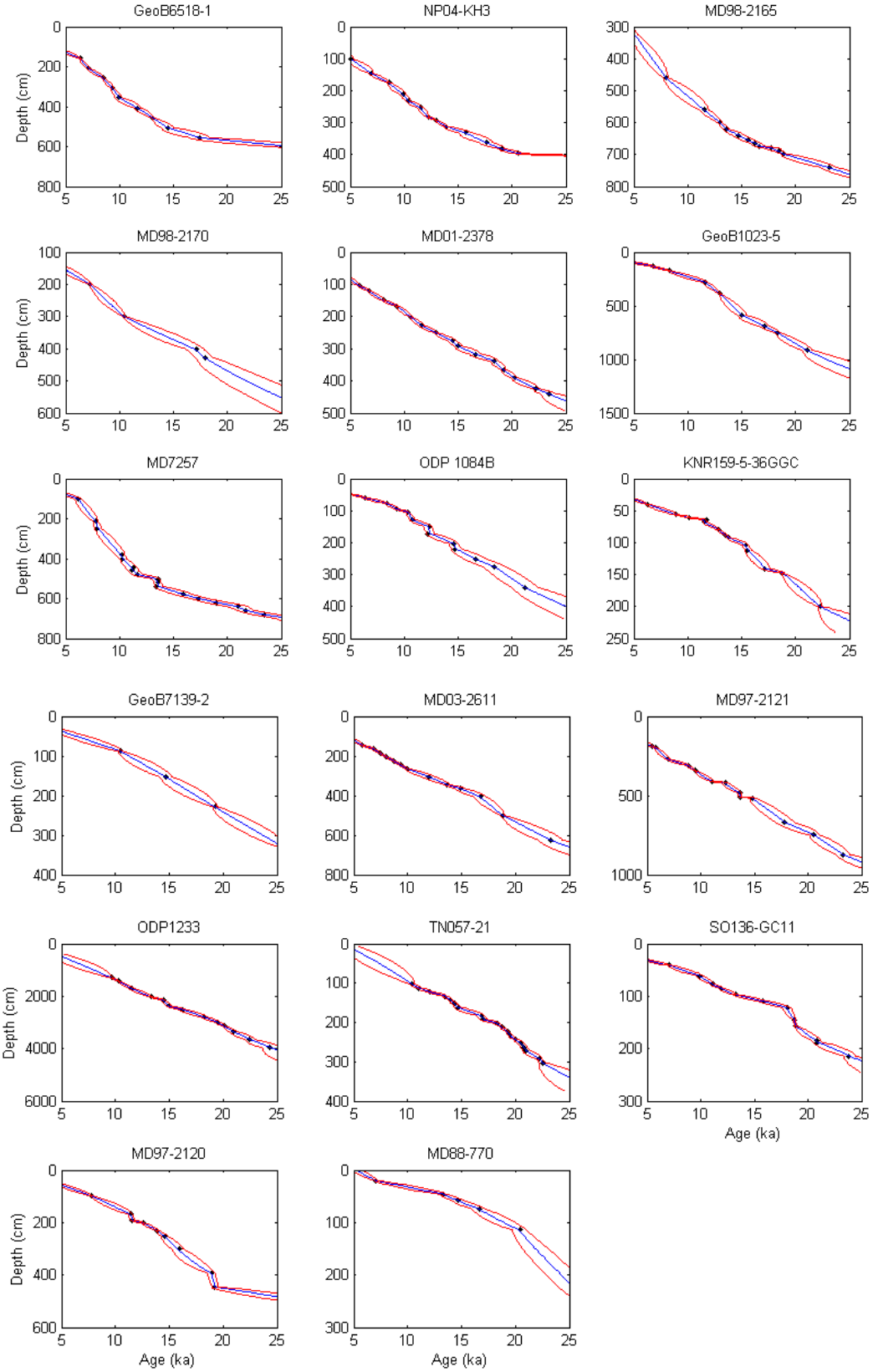
GeoB6518-1
NP04-KH3
MD98-2165
MD98-2170
MD01-2378
GeoB1023-5
MD7257
ODP 1084B
KNR159-5-36GGC
GeoB7139-2
MD03-2611
MD97-2121
ODP1233
TN057-21
SO136-GC11
MD97-2120
MD88-770
Depth (cm)
Age (ka)

Proxy temperature record plots: Proxy temperature records (blue) with 2σ uncertainties (red lines) reflecting both chronological and proxy calibration uncertainties.

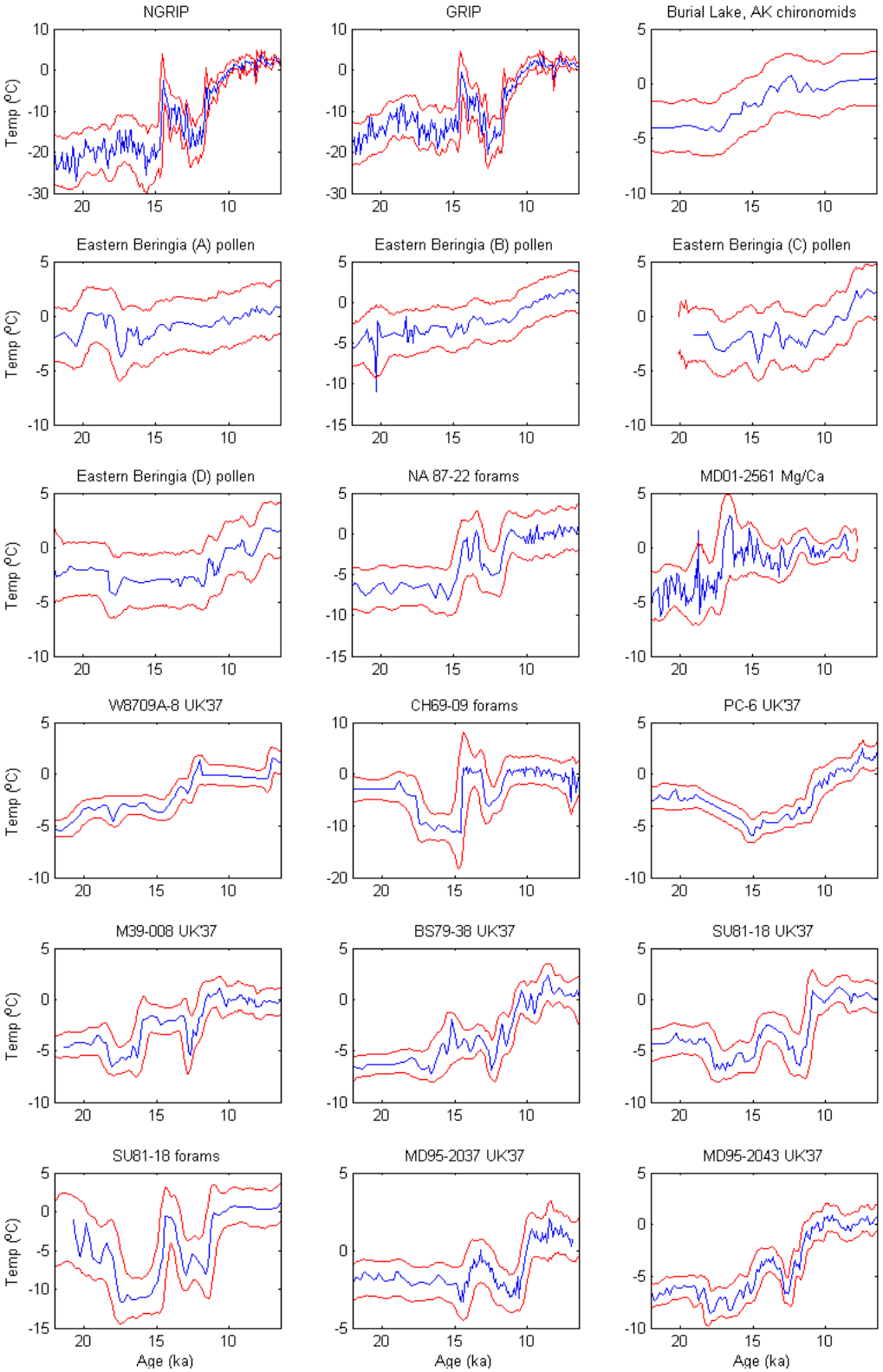

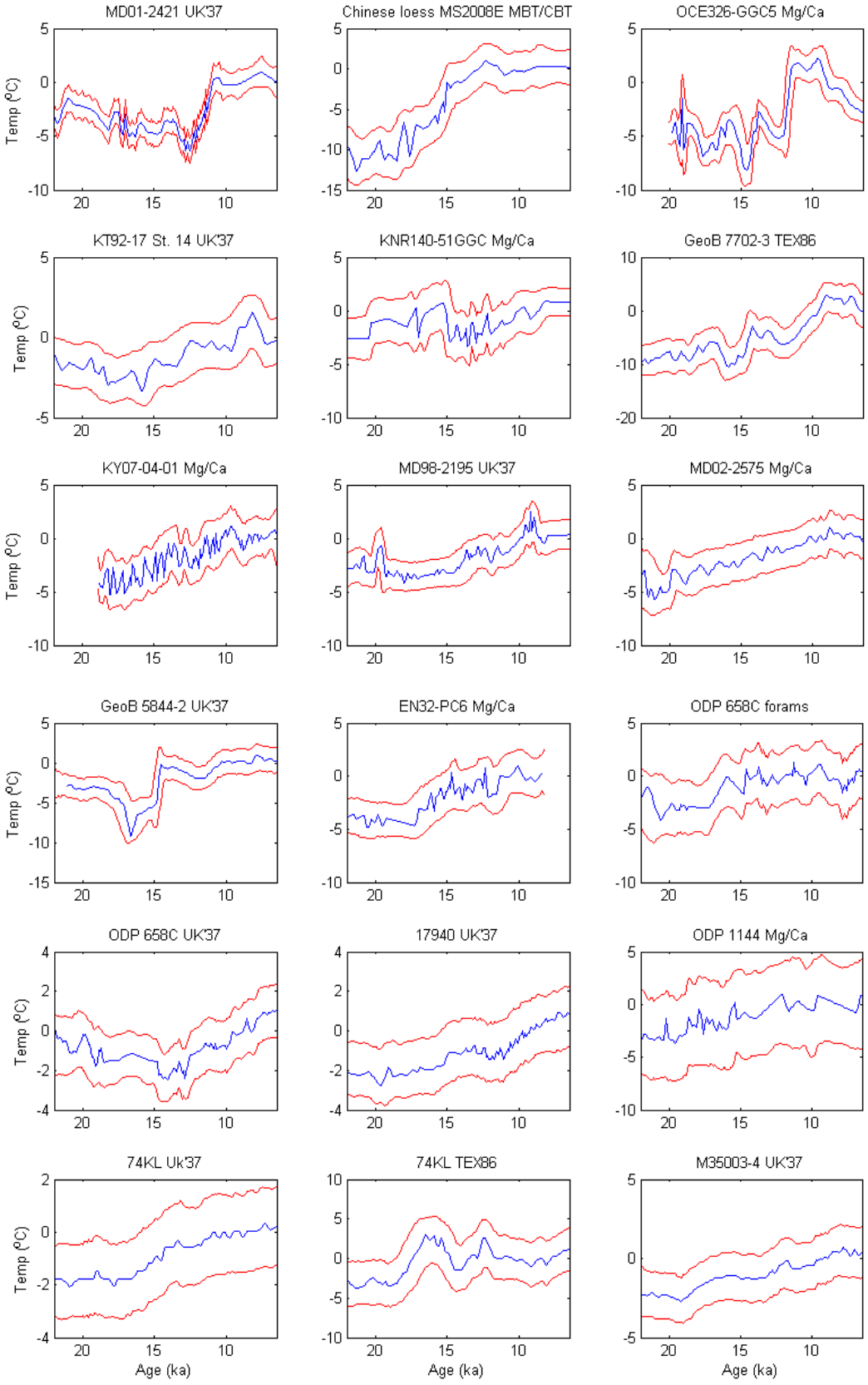
MD01-2421 UK'37
Chinese loess MS2008E MBT/CBT
OCE326-GGC5 Mg/Ca
KT92-17 St. 14 UK'37
KNR140-51GGC Mg/Ca
GeoB 7702-3 TEX86
KY07-04-01 Mg/Ca
MD98-2195 UK'37
MD02-2575 Mg/Ca
GeoB 5844-2 UK'37
EN32-PC6 Mg/Ca
ODP 658C forams
ODP 658C UK'37
17940 UK'37
ODP 1144 Mg/Ca
74KL Uk'37
74KL TEX86
M35003-4 UK'37
Temp (°C)
Age (ka)

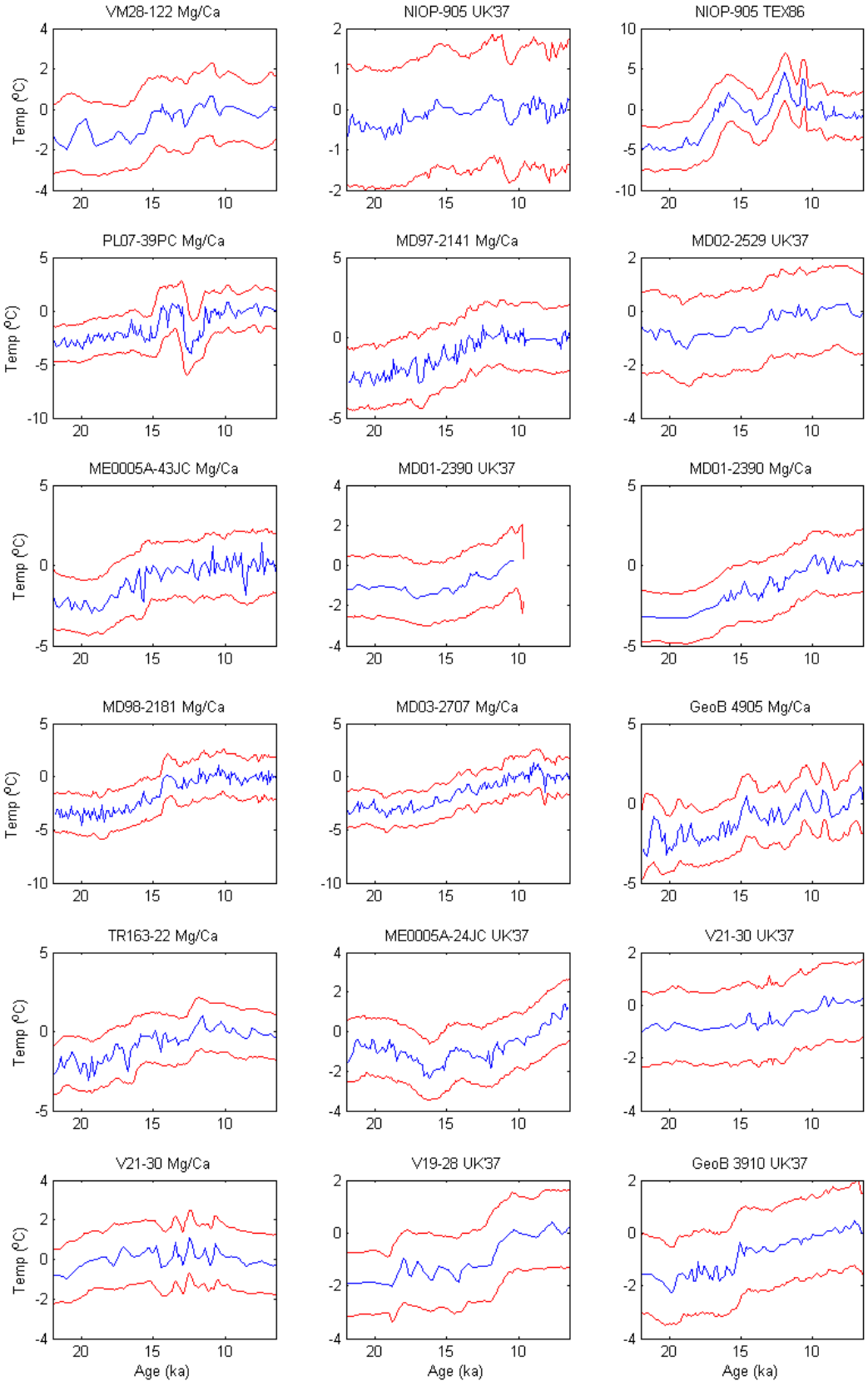
VM28-122 Mg/Ca
NIOP-905 UK'37
NIOP-905 TEX86
PL07-39PC Mg/Ca
MD97-2141 Mg/Ca
MD02-2529 UK'37
ME0005A-43JC Mg/Ca
MD01-2390 UK'37
MD01-2390 Mg/Ca
MD98-2181 Mg/Ca
MD03-2707 Mg/Ca
GeoB 4905 Mg/Ca
TR163-22 Mg/Ca
ME0005A-24JC UK'37
V21-30 UK'37
V21-30 Mg/Ca
V19-28 UK'37
GeoB 3910 UK'37
Temp (°C)
Age (ka)

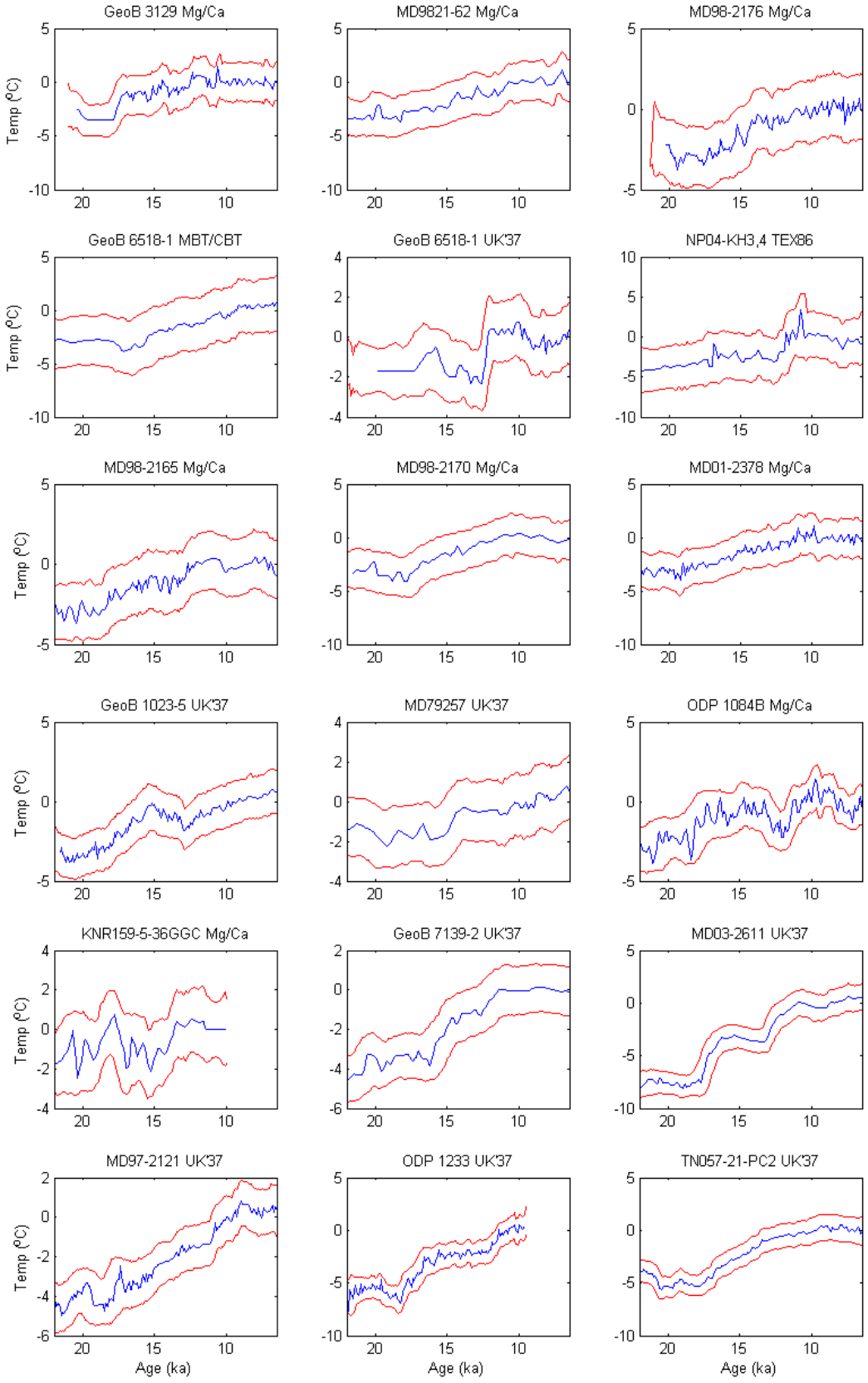
GeoB 3129 Mg/Ca
MD9821-62 Mg/Ca
MD98-2176 Mg/Ca
GeoB 6518-1 MBT/CBT
GeoB 6518-1 UK'37
NP04-KH3,4 TEX86
MD98-2165 Mg/Ca
MD98-2170 Mg/Ca
MD01-2378 Mg/Ca
GeoB 1023-5 UK'37
MD79257 UK'37
ODP 1084B Mg/Ca
KNR159-5-36GGC Mg/Ca
GeoB 7139-2 UK'37
MD03-2611 UK'37
MD97-2121 UK'37
ODP 1233 UK'37
TN057-21-PC2 UK'37
Temp (°C)
Age (ka)

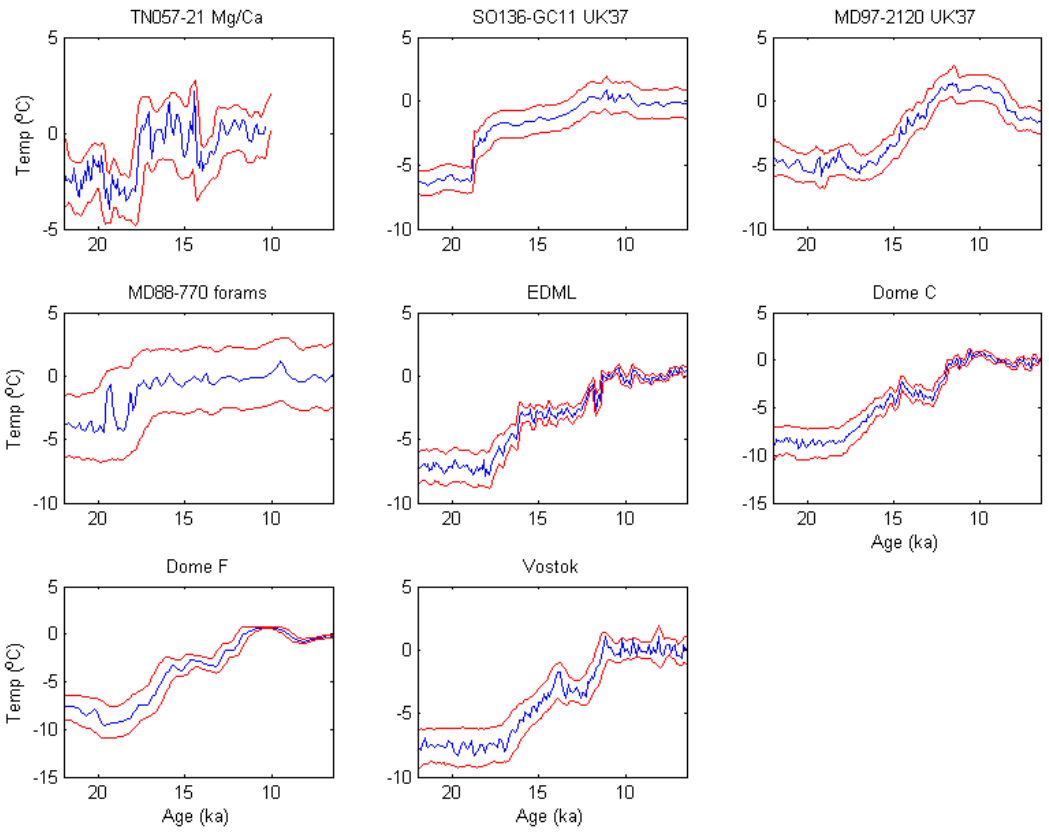
TN057-21 Mg/Ca
SO136-GC11 UK'37
MD97-2120 UK'37
MD88-770 forams
EDML
Dome C
Dome F
Vostok
Temp (°C)
Age (ka)